NOVEL MATERIALS AND DEVICES FOR ENERGY STORAGE

by

Haritha Sree Yaddanapudi

A thesis submitted to the faculty of
The University of Utah
in partial fulfillment of the requirements for the degree of

Master of Science

Department of Materials Science and Engineering

The University of Utah

December 2016

The University of Utah Graduate School

STATEMENT OF THESIS APPROVAL

The thesis of **Haritha Sree Yaddanapudi**

has been approved by the following supervisory committee members:

Ashutosh Tiwari	, Chair	7/14/2016 Date Approved
Reaz A Chaudhuri	, Member	08/01/2016 Date Approved
Jules John Magda	, Member	7/14/2016 Date Approved

and by **Feng Liu** , Chair/Dean of

the Department/College/School of **Materials Science and Engineering**

and by David B. Kieda, Dean of The Graduate School.

ABSTRACT

An increase in the demand for clean and sustainable energy storage with a high power density, along with a long cyclic life time has made supercapacitors an emerging energy storage device. However, one of the main challenges of today's world is to develop energy storage devices which are environmental friendly, cost effective, and which posses an excellent storage capacity. Therefore, this thesis presents the experimental results of utilizing nickel nanoparticle impregnated carbonized wood as a potential electrode material for supercapacitor applications. The electrode was synthesized by carbonizing the nickel nitrate impregnated wood at 900^oC for an hour. The concentration of nickel nanoparticles in the carbonized wood was varied by changing the concentration of nickel nitrate solution. The surface morphology and the structure of the electrodes as prepared were studied by using X-ray Diffraction (XRD), Scanning Electron Microscopy (SEM), Transmission Electron Microscopy (TEM), and X-ray Photoelectron Spectroscopy (XPS). Electrochemical characterization such as Cyclic Voltammetry showed the presence of peaks indicating a psuedocapacitive behaviour of the electrode. The Galvanostatic charge-discharge measurements showed nonlinear charge-discharge curves with changes in the slope. From the electrochemical measurements, it is observed that the electrode material exhibited a specific capacitance of 3616 F/g and a power density of 30 kW/kg along with an excellent capacitance retention of greater than 80% after 6000 charge-discharge cycles. These results indicate that the nickel nanoparticle impregnated carbonized wood could be one of the potential electrode materials for supercapacitor applications.

CONTENTS

LIST OF FIGURES

LIST OF TABLES

ACKNOWLEDGMENTS

Firstly, I would like to express my sincere gratitude to my advisor Dr. Ashutosh Tiwari for his continuous support, motivation, and comments throughout my MS study. His guidance helped me throughout my research. He is one of the best mentors that anyone could ask for.

Secondly, I would like to thank my committee members Dr. Reaz Chaudhuri and Dr. Jules Magda for their valuable suggestions and continuous encouragement. Furthermore, I would like to thank Dr. Shrikant Saini and Kun Tian for their continuous discussion throughout my research.

I would also like to thank all the group members of Nanostructured Materials Research Laboratory, especially David, Gene, Megan, and Yinong, for their friendship and encouragement. I would like to express my sincere gratitude to my friends Supreet, Sarvani, Sowmiya, Sahiti and Karthik for bearing me and helping me in all these two years. Last but not the least, I thank my parents and my brother for their love, support and belief in me throughout the MS study here at the University of Utah.

CHAPTER 1

INTRODUCTION

Owing to the fast development of the global economy there is a huge demand for the consumption of energy. However, due to the limited availability of fossil fuels for future consumption and increase in environmental pollution, there is a need for the development of clean, sustainable, and renewable energy resources. These renewable resources generate energy intermittently and hence we need storage devices which can store this energy generated (1-3). Some of the alternative energy storage devices which have gained most prominent research are Li-ion batteries, fuel cells, and electrochemical capacitors.

Although there is much research emphasis on Li-ion batteries and fuel cells due to their high energy density and low self-discharge rate, they lack in their poor power density and high maintenance cost (4-6). Recently, other alternative devices, such as supercapacitors, have gained much importance due to their high power capability, long cyclic life time and low maintenance cost (7-10). Furthermore, supercapacitors are classified into electrical double-layer capacitors (EDLCs), psuedocapacitors, and hybrid capacitors (11). EDLCs achieves their capacitance by storing its energy in the form of charge at the electrode-electrolyte interface, that is at the Helmholtz double layer, whereas the psuedocapacitor stores its energy in the form of surface redox reactions of an electroactive material at a certain definite potential (12). Due to the surface reaction being one of the main reasons for energy storage in a psuedocapacitor, there is every need to control the surface morphology, pore size distribution and specific surface area of the electroactive material. Recent research provides an insight that the supercapacitors have an energy density of about 3-5 W.h/kg, which is an order less than the commercialized lithium-ion batteries (13,14). Thus, a maximum energy density with a high power density is a major topic of research in the supercapacitors.

In order to understand the advantages of supercapacitors over the current commercialized energy storage devices, that is, capacitors, batteries, and fuel cells, each one of these devices is explained in detail in this chapter. Furthermore, a brief comparison on energy and power density, charge storage mechanism between these devices and the supercapacitors is

also discussed.

1.1 Capacitors

A capacitor is a passive electrical device which stores energy in the form of an electric field generated between two parallel plates, called electrodes, due to the presence of an opposite charges on them. The capacitor can release its energy very fast due to its high power density, yet the energy stored is minimal.

A conventional capacitor contains two electrodes separated by a dielectric material, as shown in Figure 1.1. In a neutral condition, that is, when no external voltage is applied between the electrodes, there are an equal number of free electrons available on both the electrodes. However, upon applying external voltage, an equal number of electrons are removed from one electrode and deposited onto the other electrode. As a result, an electric field is generated which allows the energy to be stored in the device. During the process of generating an electric field, no electron passes through the dielectric or the insulating material.

A typical parameter which characterizes the capacitor is capacitance. Capacitance is defined as the ratio of the charge stored (Q) to the applied voltage (V) and is given by

$$C = \frac{Q}{V} \tag{1.1}$$

For a capacitor containing two parallel plates with surface area A separated by a dielectric material whose dielectric constant is ϵ and thickness d, then the capacitance is given by

$$C = \frac{\epsilon A}{d} \tag{1.2}$$

Thus, the capacitance of a capacitor not only depends on the applied voltage but also depends on the dielectric material. To obtain a high capacitance, the dielectric material should possess a high dielectric constant and smaller thickness. According to the recent reports (15-19), one of the potential electrode materials is carbon-related materials. These include carbonized wood, saw dust, activated carbon, aerogels, carbon nanotubes, and graphene. The porous structure and high specific surface area of the electrode material are some of the important advantages of carbon materials which help in contributing a high storage capability with a limited size.

The important characteristics which govern any energy storage device are power density (P) and energy density (E). Generally, the energy and power densities are either given by per unit mass or per unit volume. The energy density of a capacitor, that is, the amount of

energy stored per unit mass, is given by,

$$E = \frac{CV^2}{2} \tag{1.3}$$

The power density is the duration of time (dt) taken to discharge the capacitor and is given by

$$P = \frac{dE}{dt} \tag{1.4}$$

A typical capacitor usually has a high power density anywhere higher than 5000 W/kg and a lower energy density between 0.01 W.h/kg to 0.1 W.h/kg (20). The capacitors also have a high charge and discharge capabilities when compared to the batteries and fuel cells. However, these devices do not have a capability to store large amounts of energy.

1.2 Batteries

The most common energy storage device that we find in an electronic device is the battery. A typical battery usually contains two or more electrochemical cells which are joined together. Each of these cells contains a positive and a negative electrode, called a cathode and an anode, which are separated by an electrolyte as shown in Figure 1.2. Generally, in batteries a redox reaction occurs between the electrodes, that is, the reduction at the cathode and the oxidation at the anode generating DC electricity. In other words, the chemical energy that is stored in the cells is converted into an electrical energy.

Batteries are divided into two types based on their ability to charge. There are rechargeable batteries and disposable batteries. Most of the disposable batteries include zinc-carbon and alkaline batteries which can irreversibly convert the chemical energy into electrical energy. However, the rechargeable batteries such as the Lithium-ion, Nickel-Cadmium, Sodium-ion, nickel metal hydride batteries can convert back to the original composition on subsequent charging cycles. Therefore most of the disposable batteries have a lower energy density when compared to the rechargeable batteries.

Most of the recent research is focused on the Li-ion batteries, which are the best electrochemical capacitors available in the market (21). Li-ion batteries have an energy density 10 W.h/kg - 100 W.h/kg and power densities of 100 W/kg - 1000 W/kg (20). Additionally, the Li-ion batteries are moderate in weight and have no memory effect. However, memory effect is observed in rechargeable batteries like nickel-cadmium and nickel-metal hydride. Although the Li-ion batteries have a high specific energy, they lack in their charging and discharging rates. Moreover, the Li-ion batteries have a low power density when compared to the other energy storage devices.

1.3 Fuel Cells

As the name suggests, fuel cells are the devices which convert chemical energy from a fuel into electrical energy through a chemical reaction occurring between the hydrogen ions and oxygen. The byproduct of the fuel cells is heat and water. Unlike the batteries, these fuel cells cannot be recharged and can continuously work until fuel and oxidizing agent for chemical reaction to occur is exhausted.

Most of the fuel cells do not require any intermediate combustion steps, such as thermomechanical methods. Additionally, these cells have a high energy conversion efficiency of 40%-60% (22,23). Owing to the above-mentioned advantages, fuel cell technology is one of the clean, environmental friendly, economical, and reliable sources of energy storage devices. When compared to all the available energy storage devices, fuel cells have a high energy density, between 100 W.h/kg- 1000 W.h/kg. However, the power density of these devices is minimal, restricting them in the use of high power applications (20).

Conventional fuel cells contain an anode, cathode, and electrolyte. The electrolyte helps in the movement of the ions from one side of the cell to the other. The anode and cathode contain a catalyst which helps the fuel to undergo the oxidation process (23). The working of a fuel cell is illustrated in Figure 1.3. Depending on the type of the electrolyte the fuel cells can be varied. The various types of electrolytes are aqueous alkaline solution, polymer membrane, and ceramic oxide.

The most common fuel cell that is observed is the Hydrogen Proton Exchange membrane (PEM) fuel cell. A PEM fuel cell usually contains hydrogen which is moved to the anode. A catalyst is introduced such that it can oxidize the hydrogen into protons (Hydrogen ions) and electrons. A PEM fuel cell is designed in such a way that all the electrons move towards the anode and the protons towards the cathode. When an external load is applied, the electrons travel towards the protons through the external circuit. Consequently, these electrons combine with the protons in the presence of oxygen, generating DC electricity with either heat or water as a byproduct.

1.4 Supercapacitors

Although, the batteries and the fuel cells have a high specific energy, their low power density limits their usage in high-power applications. Hence, research on alternative devices such as supercapacitors with high energy and power density is gaining more emphasis. Like the capacitors, supercapacitors also have two electrodes separated by a dielectric material. However, the only difference between the capacitor and the supercapacitor is that the surface area of the supercapacitors is high and also the distance between the electrodes is smaller.

As a result, the capacitance and the energy density obtained from Equation 1.2 and 1.3 substantially increase. Additionally, these devices maintain a low equivalent series resistance (ESR), which helps in minimizing the power loss.

A conventional supercapacitor contains two electrodes immersed in an electrolyte separated by a dielectric membrane as shown in Figure 1.4. The dielectric membrane helps the ions to pass through the electrolyte. When an external voltage is applied, charges accumulate on the electrode. Due to the law of attraction of opposite charges, the charges on the electrode start diffusing through the electrolyte into the pores of the electrode. The electrodes are engineered in such a way that there is no recombination between the ions. As a result, a double-layer is formed at each of the two electrodes. To achieve a high energy and power density, the electrode material should be porous with a high surface area and there should be a smaller distance between the electrodes. A more detailed discussion about different types of supercapacitors and their energy storage mechanisms can be found in Chapter 2.

1.5 Comparison of Energy Storage Devices

The performance of various energy storage devices can be studied by using a Ragone Plot. A Ragone Plot is a chart which compares energy density and power density of the devices represented on the X-axis and Y-axis, respectively, as shown in Figure 1.5 (20). From Figure 1.5, it can be inferred that the capacitors have a high power density but relatively low energy density when compared to the supercapacitors and batteries. In other words, the capacitors can be charged and discharged quickly, yet the energy stored is very minimal. On the other hand, batteries and fuel cells have a high energy density and low power density when compared to supercapacitors. Furthermore, they take a longer time to charge and discharge. Hence, to overcome the drawbacks, research on supercapacitors is gaining in importance.

Supercapacitors have a relatively high power density and low energy density. Additionally these devices have a high charge and discharge rates. Besides bridging the gap between the capacitors and the batteries, the supercapacitors also have several advantages, such as the charging phenomenon being reversible, that is, there is no physical or chemical change occurring during the process, and a longer cyclic life, they can be charged and discharged for at least 10,000 cycles. Moreover, the supercapacitors have less weight and less toxicity (12). Owing to these advantages, supercapacitors can be promising candidates as an alternative energy storage device.

1.6 Research and Motivation

To overcome the disadvantages of supercapacitors, research on the development of new electrolytes with a high operational voltage window, less thickness, and low permittivity is gaining in importance. Furthermore, current research also emphasis on the development of alternative electrode materials which are porous, possess high surface area and a low cost of fabrication. One such electrode material which is of interest is carbon material. Carbon materials have high conductivity, good electrochemical stability, high porosity, large specific surface area and are of moderate costs. Carbon materials are prepared from various precursors such as polymers, coal, biomass residue, and so forth (24).

In order to realize the goal of the research, we use the biomass-based material, that is, wood, to reduce the cost of fabrication. Apart from the low cost, the wood structure has a high porosity with large specific surface area (25-29). Additionally, to enhance the performance of the supercapacitor, which is defined by its capacitance, energy density, and power density, we utilize nickel nanoparticles as a precursor material which is impregnated into the carbonized wood which is then used as an electrode in the supercapacitor cell.

In this thesis, a facile preparation of nickel nanoparticle impregnated carbonized wood composite used as an electrode material for supercapacitor application is reported. Electrochemical characterization techniques such as Cyclic Voltammetry, Electrochemical Impedance Spectroscopy and galvanostatic charge-discharge measurements are conducted. It was observed that the nickel nanoparticle impregnated carbonized wood electrode achieved a specific capacitance of about 90.4 F/g at 2 M concentration, with retention of 92% after 1000 cycles. Moreover, a power density of as high as 750 W/kg with a corresponding energy density of 3.14 W.h/kg was obtained.

1.7 Organization of Thesis

The rest of the thesis is organized into the following chapters.

Chapter 2, Principles of Energy Storage in Supercapacitors, discusses different types of supercapacitors and their underlying mechanisms followed by their advantages and disadvantages.

Chapter 3, Facile Preparation of Nickel/Carbon Based Composite as Electrodes for Supercapacitors, discusses the facile synthesis technique of nickel/carbon composite electrode. This is followed by the material characterization results. The material characterization techniques mainly involve X-ray diffraction, Scanning Electron Microscopy, Transmission Electron Microscopy, and X-ray photoelectron spectroscopy.

Chapter 4, Electrochemical Characterization of Nickel/Carbon-based Composite electrodes, discusses the effect of varying nickel nanoparticles concentration on electrochemical properties in carbonized wood. The electrochemical characterization methods include Cyclic Voltammetry, Electrochemical Impedance Spectroscopy, and galvanostatic charge-discharge. Furthermore, a comparison of the fabricated electrode with present day available energy storage devices in terms of specific capacitance, energy density, and power density is also discussed.

Chapter 5, Conclusion and Future Work, discusses a brief summary of the results based on the experiments that were conducted followed by some suggestions for future works.

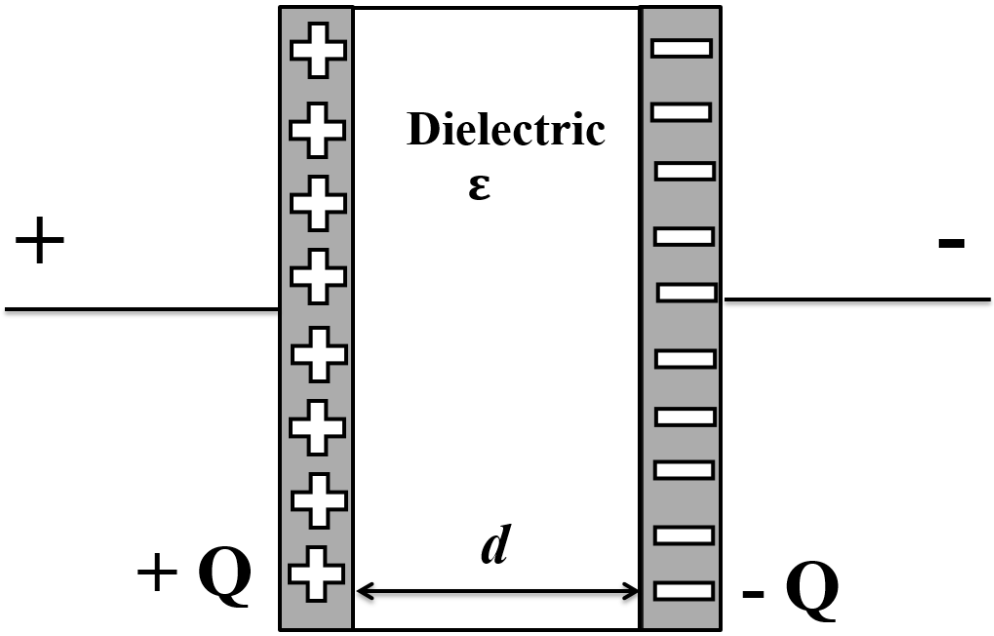

Figure 1.1. Schematic diagram of an electrostatic capacitor. Capacitors store energy in the form of electric field generated between two parallel plates.

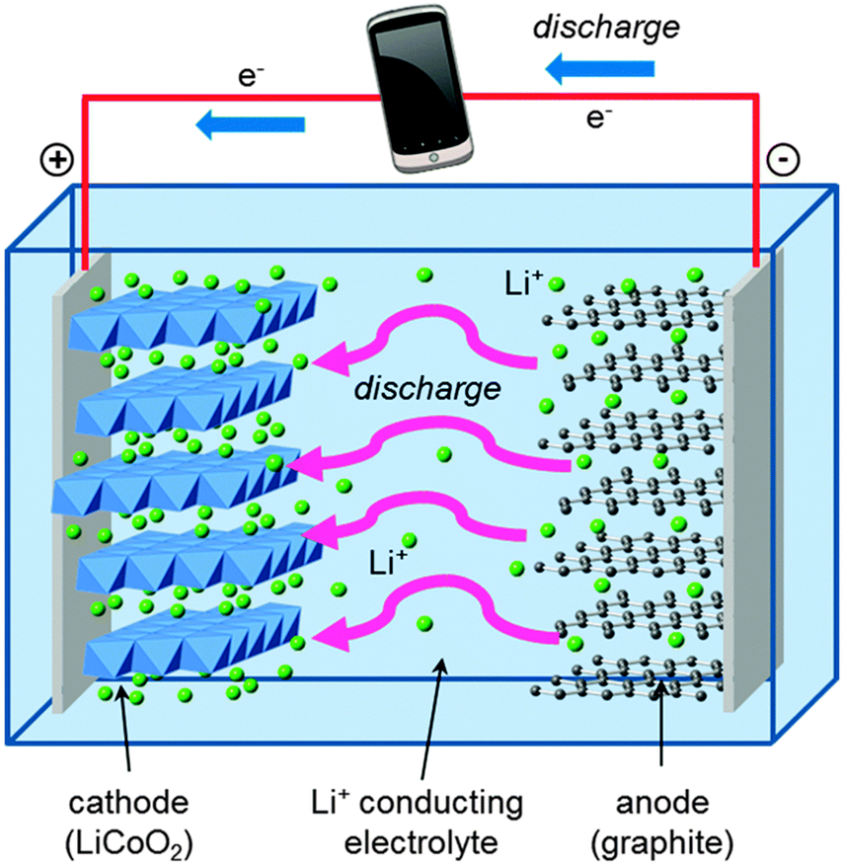

Figure 1.2. Schematic diagram of a Li-ion battery. During charging, lithium ions flow to the negative electrode through the electrolyte and electrons flow from the external circuit. During discharge the directions are reversed, generating useful power to be consumed by the device (30).

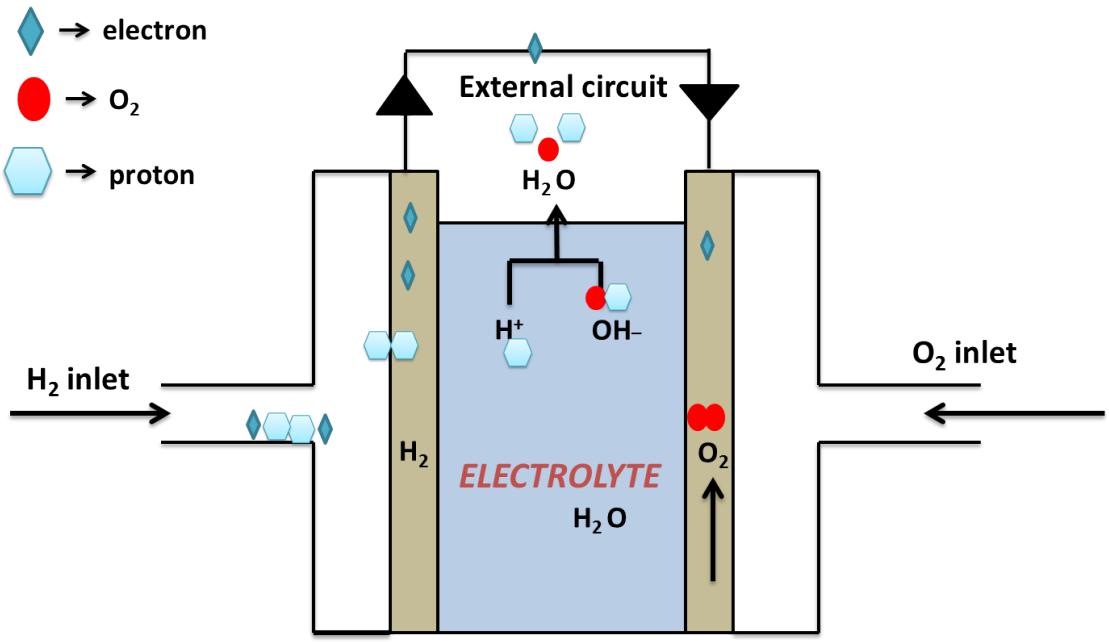

Figure 1.3. Schematic illustration of the working principle of a Fuel Cell. Oxygen and hydrogen are the two fuel cells used in this case which produce water (and heat) as the products. The hydrogen is fed to one of the electrode, where it is oxidized into H^+ ions. The oxygen is fed to the opposite electrode, where it is reduced to OH^- ions through reaction with water in the electrolyte. Both those ions meet in the electrolyte between the two electrodes to form water. During this process, the electrons taken from the hydrogen are taken into an external electric circuit before returning to the cathode to form the OH^- ions (23).

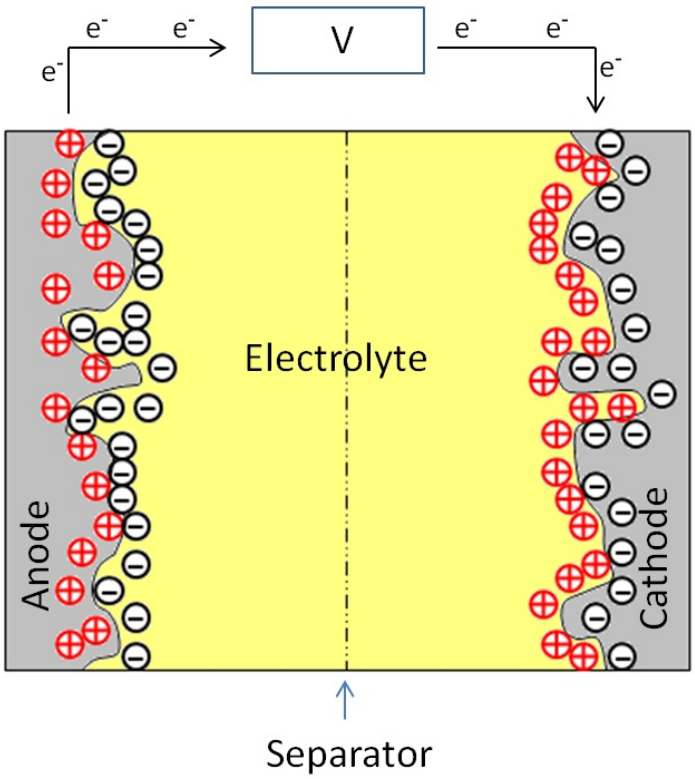

Figure 1.4. Schematic diagram of a supercapacitor (31). During charging, when an external voltage is applied, the double-layer created results in charge-storage.

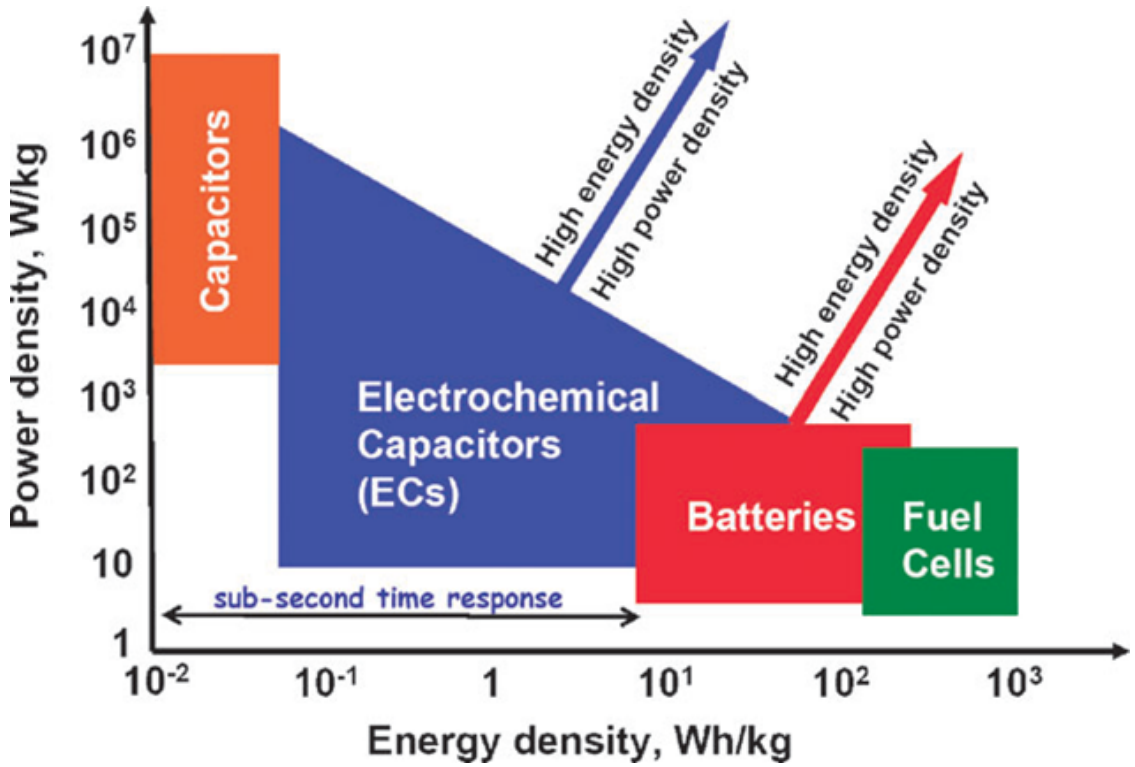

Figure 1.5. Ragone plot showing the energy and power density for various energy storage devices (20).

CHAPTER 2

PRINCIPLES OF ENERGY STORAGE IN SUPERCAPACITORS

Based on the type of charge-storage mechanism, electrochemical supercapacitors are classified into electrochemical double-layer (EDL) capacitors, psuedocapacitors, and hybrid capacitors, as shown in Figure 2.1. Each of these will be discussed further in this chapter as follows.

2.1 Electrochemical Double-Layer Capacitors

An EDL capacitor utilizes the electrostatic energy stored in the Helmholtz double layer, which is formed between the electrode and electrolyte. To understand the principle of energy storage in an EDL capacitor, one needs to know the concept of the double layer formation, which is utilized to visualize the ionic environment around the vicinity of the electrode material/charged surface. Three different models are used to describe the concept of double layer further. They are the Helmholtz model, the Gouy-Chapman model, and the Stern model.

2.1.1 Helmholtz Model

The helmholtz double-layer model is the simplest model which describes the distribution of opposite charges quasi-2-dimensionally occurring first at the interface of colloidal particles (32), and is shown in Figure 2.2 (33). The helmholtz model is the simplest approximation of the surface charges which are neutralized by the counter ions and are separated by distance 'd'. As a result, there is an electrostatic ion interaction which is created between the surface and the counter ions in the solution. The surface charge potential is linearly dissipated from the surface to the counter ions satisfying the charge, as shown in Figure 2.2. The distance d corresponds to the center of the counter ions, that is, their radius.

The main drawback of this model is that the ions on the solution side of the double layer will not remain static in a compact array as in Figure 2.2 but are subjected to thermal

fluctuations. Furthermore, this model does not take ion diffusion, adsorption onto the surface and solvent/surface interactions into account (34,35).

2.1.2 Gouy-Chapman Double-Layer Model

The Gouy-Chapman model utilizes the thermal fluctuations factor, which is one of the drawbacks of the Helmholtz model. In this model, Gouy suggested that the interfacial potential is due to the charged ions on the surface which are fixed to the electrode, developing a double-layer. These ions are further surrounded by an equal number of opposite ions which diffuse through the electrolyte as illustrated in Figure 2.2 (33). The kinetic energy of the diffused ions will affect the thickness of the double layer. However, the Gouy model has its own limitations, such as the assumption of point charges, which is false and has led to incorrect potential profile and local field near the electrode surface and, consequently, an excessively large double-layer diffusive capacitance (36). Later, Gouy and Chapman together defined the diffuse double layer model in which the diffused ions follow the Boltzmann distribution and Poisson equation.

However, the Gouy-Chapman model has certain drawbacks. For one thing, it overestimates the double layer capacitance, leading to a decrease in the accuracy. Secondly, it assumes that the ions are point charges, which is not true. Furthermore, it assumes there are no physical limitations for the ions to approach towards the surface, which is not correct.

2.1.3 Stern Model

The Stern model modified the Gouy-Chapman diffusive double-layer model by overcoming its drawbacks. According to the Stern model, the ions are no longer point charges but instead they have a finite size. Furthermore, the ions are not fixed to the surface but at a distance δ. The layers of the ions are placed at a distance from the surface known as the stern layer and are surrounded by the counter ions. This is illustrated in Figure 2.2 (33).

The surface charge σ_s is balanced by the sum of the double-layer charge $\sigma_s$dl and stern layer charge σ_s δ. The surface potential ψ_s depends on the electrolytic concentration and the surface charge.

2.2 Psuedocapacitors

Unlike the EDL capacitors, the psuedocapacitors are complemented by psuedocapacitance, which occurs mostly due to the faradic reactions like electrosorption, redox reaction and intercalation processes. Psuedocapacitance mainly involves the passage of the charge across the double layer, but the capacitance originates due to the faradic reactions. It

arises only when the extent of reaction Q that is given in terms of charge storage is a function of potential V. Furthermore, Q/V measures the capacitance of the psuedocapacitor. Moreover, psuedocapacitance can also arise due to the Warburg impedance associated with the diffusion-controlled process which varies with the AC modulation and is inversely proportional to the square root of the frequency. The faradic reactions and the Warburg impedance allow the psuedocapacitor to have a high energy density along with a good specific capacitance.

2.3 Hybrid Capacitors

Hybrid capacitors utilize the advantages of EDL capacitors and mitigate the disadvantages of the psuedocapacitors to improve their performance. Additionally, the hybrid capacitors use both faradic and nonfaradic charge storage mechanisms to store energy. The energy density and power density of the hybrid capacitors are larger than the EDLCs and do not disturb the cyclic stability and affordability of the hybrid capacitor. The hybrid capacitors can be distinguished based on their electrode configuration, which can be either a composite type, asymmetric type, or battery type. A composite type electrode material integrates the carbon-based materials with metal oxides and conducting materials and incorporates both physical and chemical changes during the charge storage mechanism. Asymmetric type electrode materials integrate the EDLCs with the psuedocapacitors and utilize the faradic and nonfaradic reactions as the charge storage mechanisms.This asymmetric type of hybrid capacitor have a high energy density and power density when compared to the composite type or a battery type of hybrid capacitor.

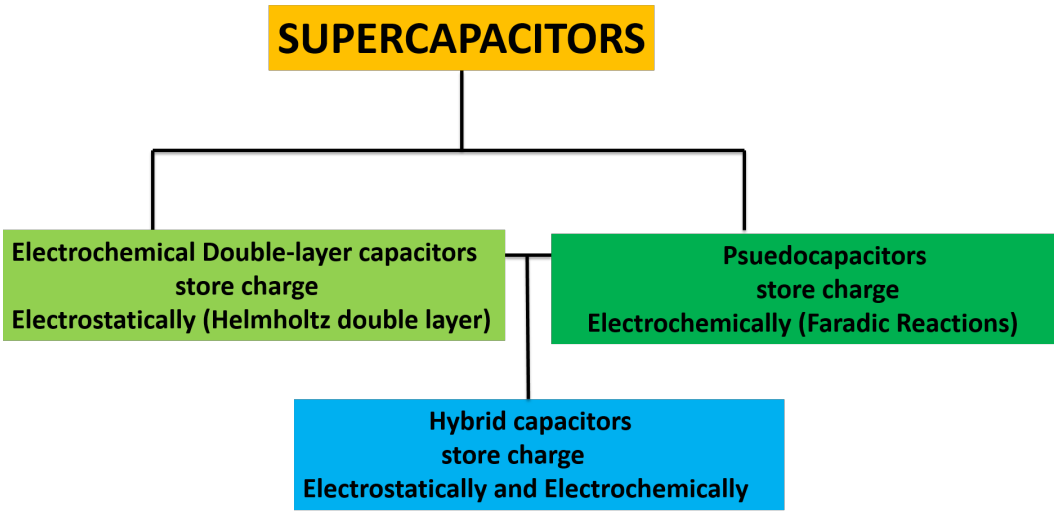

Figure 2.1. Schematic illustration of classification of electrochemical supercapacitors. Based on the charge-storage mechanism, supercapacitors are divided into electrochemical double-layer capacitors, psuedocapacitors, and hybrid capacitors.

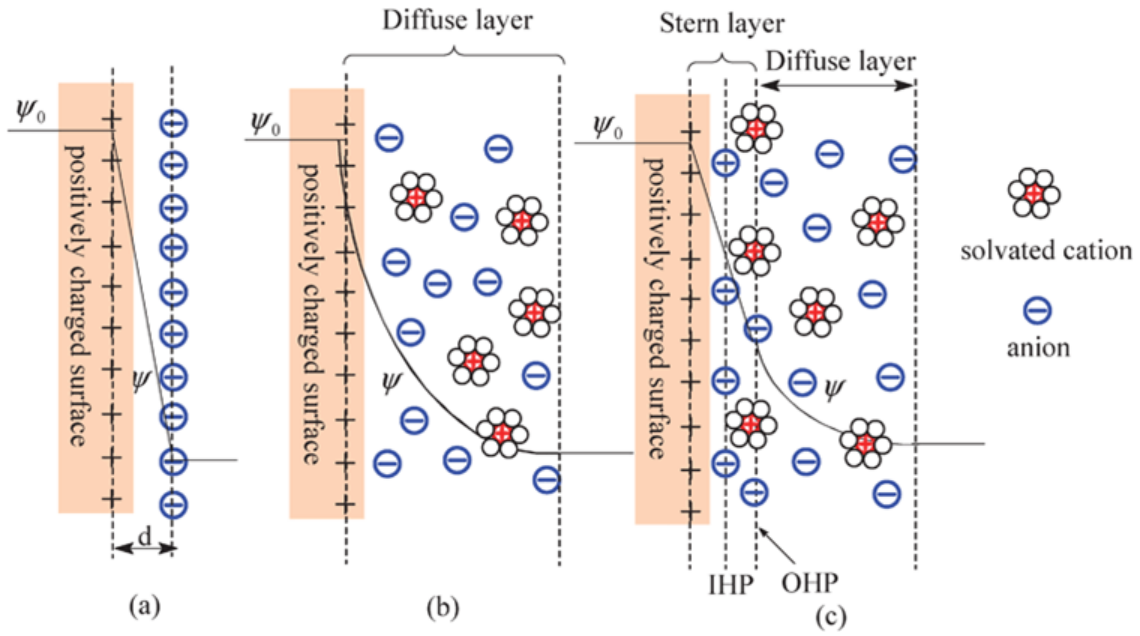

Figure 2.2. Schematic diagram of models of the electrical double layer at a positively charged surface: (a) the Helmholtz model, (b) the Gouy-Chapman model, and (c) the Stern model (33).

CHAPTER 3

FACILE PREPARATION OF NICKEL-CARBON BASED COMPOSITE AS ELECTRODES FOR SUPERCAPACITORS

A few important requirements for an electrode material to be utilized for supercapacitor applications are high surface area, large porosity, chemical stability, high electrical and ionic conductivities, and biodegradability. One of the electrode materials satisfying these requirements is carbonized wood. To improve the capacitance of carbonized wood electrodes, psuedocapacitive materials such as nickel nanoparticles of varying concentration are added. Herewith, a facile synthesis process for nickel nanoparticle impregnated carbonized wood is discussed. Material characterization techniques such as scanning electron microscopy, X-ray diffraction, transmission electron microscopy, and X-ray photo-electron spectroscopy are also discussed.

3.1 Preparation of Nickel Nanoparticle Impregnated Carbonized Wood Electrodes

Firstly the precursor material, beech wood, is initially cut into disc-shaped samples and rinsed under running water to remove the sawdust. The washed wood pieces are then boiled in 1 M ammonia solution at 90^oC for 5 hours. This helps in removing the resins and additional impurities present in the wood. The outer bark of the boiled wood samples is later removed and the wood pieces are then transferred into a box furnace for dehydration process occurring at a temperature of 120^oC for 3 hours. The dehydrated wood samples are then immersed in nickel nitrate hexahydrate solution for 4 hours at 90^oC. The concentration of nickel nitrate solution is varied from 0.5 M to 3 M and the samples are designated as Ni 0.5 M, Ni 1 M, Ni 2 M, Ni 3 M. The immersion of wood in nickel nitrate hexahydrate solution helps in impregnating the nickel nitrate ions into the pores of the dehydrated wood sample. The nickel nitrate impregnated wood samples are then transferred into a tube furnace for carbonization at 900^oC under N_2 atmosphere for an hour. The carbonization process helps

in formation of nickel nanoparticles by the reduction of nickel nitrate. Thus, the nickel nanoparticle impregnated carbonized wood samples are used for testing. Figure 3.1 shows the schematic diagram of the preparation of nickel nanoparticle impregnated carbonized wood samples.

3.2 Materials Characterization

3.2.1 Determination of Nickel Content in Nickel Nanoparticles Impregnated Samples

The nickel nanoparticle impregnated carbonized wood samples are initially cut into two halves, of which one half is used in determining the amount of nickel and the other half is used for further testing. The initial weight of one half of the sample is taken and is denoted as 'W_1'. The sample is then transferred into a box furnace where all the samples were heated to 900^oC in air for 4 hours to convert all the carbon present in the sample into carbon dioxide and nickel to nickel oxide. The weight of the sample after burning into nickel oxide is weighed and denoted as 'W_2'. From the amount of nickel oxide that is formed we calculate the weight of nickel present in the sample by using the molecular weight of nickel and the molecular weight of nickel oxide. The amount of nickel content in the samples is estimated by using Equation 3.1 and is tabulated in Table 3.1.

$$\%Ni = \frac{78.6 \times W_2}{W_1} \tag{3.1}$$

3.2.2 X-ray Diffraction

X-ray diffraction (XRD) is a quantitative and nondestructive technique used to characterize the sample in terms of its composition and crystal structure.

A crystal lattice is a three-dimensional arrangement of atoms and ions in an ordered and symmetrical system that are repeated at regular intervals. During the repetition, the order and symmetry are kept constant. This symmetry is often separated by parallel planes with distance 'd' , which varies with the type of material. This 'd'spacing also changes with respect to the specific crystalline planes. According to Bragg's law, which is the principle of XRD, when an X-ray is incident onto this crystal lattice surface, an optical diffraction occurs when a monochromatic X-ray beam constructively interferes with the lattice. By changing the 'd' spacing, the Bragg's angle also changes as seen in equation 3.2. A typical XRD pattern is obtained by varying the intensity with the angle 'θ '.

$$n\lambda = 2dsin(\theta) \tag{3.2}$$

XRD studies of nickel nanoparticle impregnated carbonized wood samples were performed using the Philips X'Pert PW3040 θ-2θ X-ray diffraction using Cu-K X-ray source. The X-ray beam is energized at 45 KV and 40 mA. The incident optical angle is maintained at 1^o with 1 cm slit size, a $(1/2)^o$ antiscatter slit size and $(1/4)^o$ receiving slit. XRD scans were collected from a scan rate of 0.05 s^{-1} with 2θ ranging from 10^o to 90^o. Intensity v/s 2θ XRD plots are collected and analyzed using X'Pert High Score Plus software.

Figure 3.2 shows the XRD plots of Ni 0.5 M, Ni 1 M, Ni 2 M, and Ni 3 M samples. As observed from Figure 3.2, the characteristic peaks at 44^o, 51^o and 76^o with the corresponding lattices (111), (200), and (220), respectively, indicate the presence of pure cubic nickel phase (JCPDS Reference Number 00-004-0850), whereas the characteristic peak at 26^o with the corresponding lattice (002) indicates the formation of pure hexagonal graphite (JCPDS Reference Number 00-056-0159). No other phases apart from pure cubic nickel and hexagonal graphite were formed after carbonization at 900^oC for an hour.

3.2.3 Scanning Electron Microscopy

Scanning electron microscopy (SEM) is used to study the surface morphology and phase distribution in a sample. The working principle of SEM is illustrated in Figure 3.3 (37). SEM uses a focused beam of electrons which interacts with the surface of the sample and as a result produces X-rays, secondary electrons, back-scattered electrons, and auger electrons. These are detected by the detectors which transmit the signal to the device to obtain an image.

To study the surface morphology of the nickel nanoparticle impregnated carbonized wood samples, a Hitachi 2003 SEM is used. Figure 3.4 indicates the SEM micrographs at low magnification (a) and high magnification (b). Figure 3.4 (a) shows the interconnected channels for all the samples, indicating the retention of the three-dimensional structure of the wood even after the carbonization of the wood at 900^oC. Furthermore, the SEM micrographs at high magnification shown in Figure 3.4 (b) indicate that the nickel nanoparticles are uniformly distributed in pores across and deep within the sample surface. As observed, the nickel nanoparticles size steadily increases with the increase in the concentration of nickel nitrate solution. The average nickel nanoparticles size for Ni 0.5 M, Ni 1 M, Ni 2 M, and Ni 3 M obtained from the SEM images were found to be around 171 nm, 210 nm, 299 nm, and 347 nm, respectively.

3.3 Transmission Electron Microscopy

Transmission electron microscopy (TEM) is utilized to study the surface topography, morphology, and crystallographic arrangement of atoms along with their composition and their relative amounts. The working principle of TEM is shown in Figure 3.5. TEM uses a beam of electrons which is passed through the specimen. These electrons are accelerated at high energy levels (few hundreds keV), which either scatter or back-scatter elastically or inelastically. The interaction of the electron beam with the sample results in unscattered electrons,elastic scattered electrons, and inelastic scattered electrons. Out of these interactions, unscattered electrons are mainly used in imaging the specimen. This imaging mode provides a high-magnification view of the micro- and nanostructures, resulting in high-resolution imaging. Apart from the imaging, TEM is also used to study electron diffraction, which helps to obtain accurate information about the local crystal structure.

The surface topography and morphology of the nickel nanoparticle impregnated carbonized wood samples is studied by using a TEM (JEOL JEM-2800) equipped with an energy-dispersive spectrometer (EDX). Figure 3.6 shows the bright field TEM image at (a) low magnification, and (b) high magnification. From the bright field TEM image, that is shown in Figure 3.6 (a), the dark spots which are encircled show the presence of nickel nanoparticles. Furthermore, the inset of Figure 3.6 (a) shows the selective area electron diffraction (SAED) pattern of nickel nanoparticle impregnated carbonized wood. From the SAED pattern, clearly the ring diffraction pattern shown can be indexed to (002) plane of graphite in the synthesized electrode, indicating the high conductivity of nickel nanoparticle impregnated carbonized wood. Moreover, Figure 3.6 (b) shows a high-resolution transmission electron microscopy (HRTEM) image of nickel nanoparticle impregnated carbonized wood. The HRTEM image shows a well-resolved lattice fringe with an equal interplanar distance of 0.18 nm that corresponds to the d-spacing of (200) plane of cubic phase nickel, revealing a high crystallization feature of NiNPs. To maintain the clarity in the image, the bottom inset of Figure 3.6 (b) demonstrates a simulation image of Inverse fast Fourier transformation (IFFT) taken from the enclosure region represented in the HRTEM image. The inset of Figure 3.6 shows a fast Fourier transformation (FFT) pattern collected from the area of the lattice fringes. The FFT exhibits a zone axis of [011] for NiNPs. The lattice planes of the FFT can be further indexed as (200), (11-1), and (-11-1), respectively, which are consistent with the XRD results (shown in Figure 3.2).

Apart from the surface morphology and crystallographic studies, the distribution of nickel nanoparticles in the carbonized wood has also been studied using EDS. Figure 3.7

shows the EDX images of nickel nanoparticle impregnated carbonized wood. The images shown in Figure 3.7 (a) and 3.7 (b) indicate the high-angle annular dark-field scanning transmission electron microscopy (DF-STEM) and bright-field scanning transmission electron microscopy (BF-STEM), respectively. The DF-STEM and BF-STEM images reveal a clear formation of nanoparticles in the electrode. Figure 3.7 (c) and (d) indicate the EDX mapping to study the elemental distribution in nickel nanoparticle impregnated carbonized wood electrodes. The EDX-STEM elemental mapping images shown in Figure 3.7 (c) and 3.7 (d) correspond to the K-edge signals of C, Ni collected over the electrode region. A uniform distribution of carbon with small amounts of nickel nanoparticle is clearly evident, which further demonstrates the presence of nickel nanoparticles. Figure 3.7 (e) shows the line profile across the nickel nanoparticle w.r.t to oxygen, indicated by an arrow in Figure 3.7 (d). It is clearly observed that, when there are nickel nanoparticles in the wood, the amount of oxygen surrounding it is very minimal, proving that the nanoparticles are nickel rather than nickel oxide. To further validate this, X-ray photo-electron spectroscopy measurements were performed.

3.4 X-ray Photo-electron Spectroscopy

X-ray photo-electron spectroscopy (XPS) is a surface-sensitive technique which is mainly used to measure a wide range of properties such as the elemental composition of the surface, empirical formula of pure materials, elements that contaminate the surface, chemical or electronic state of each element in the sample, line profile to determine the uniformity of composition across the sample surface, and depth profiling using ion beam etching to determine the uniformity of composition beneath the surface.

The basic mechanism behind an XPS instrument is illustrated in Figure 3.8. Photons with certain energy are mainly used to excite the electronic states of atoms. This occurs when the photons hit the electrons in the sample, and electrons with necessary energy from the atoms in the sample are ejected. These electrons are further filtered using a hemispherical analyser (HSA) before the intensity is detected by the detector. As the core-level electrons are quantized, the energy spectra exhibit peaks which correspond to different electronic structures of atom. These electrons are then analyzed by the XPS detector. The kinetic energy provides the required information to determine the elements present.

Figure 3.9 shows the high resolution XPS spectra of synthesized or uncharged sample, charged sample, and charged samples with successive mechanical etching. From the binding energies of Ni 2p peaks, the oxidation state of nickel can be found. It can be observed that

the uncharged or as prepared sample exhibits a characteristic Ni 2p peak, which corresponds to the presence of nickel in metallic state (Ni^0) with its oxidation state as 0. However, the binding energies for the charged samples shifts to a higher energy, indicating that the nickel is oxidised to a higher ionic state, that is, 2+. Furthermore, when the charged samples was mechanically etched by 0.1 mm, peaks corresponding to both the metallic phase as well as the oxidized phase were observed. Moreover, when the sample was further mechanically etched by 0.2 mm, a larger amount of nickel in metallic state rather than its oxidized state was observed. For further analyses on the ionic state of nickel, the high-resolution XPS scans were deconvoluted and resolved fitting has been performed.

Figure 3.10 shows the XPS resolved fitting peaks for (a) uncharged or as prepared samples, (b) untreated charged sample, (c) charged sample with mechanical etching of 0.1 mm, and (d) charged sample with mechanical etching of 0.2 mm. From the resolved fitting of high-resolution XPS spectrum and by using the binding energy (BE) of the Ni $2p_{3/2}$ and Ni $2p_{1/2}$ peaks, the oxidation state of nickel is assessed. It was observed that for the uncharged sample shown in (a), the peak positions of Ni $2p_{3/2}$ and Ni $2p_{1/2}$ were found to be at 852.6 eV and 869.9 eV, respectively, which corresponds to the metallic phase of nickel (Ni^0) in the electrode. Therefore, it is clearly evident that the uncharged electrode contains Ni in Ni^0 state. The corresponding satellite peaks of nickel shown in Figure 3.10 are represented by 'S'. Contrary to the uncharged sample, the charged sample shown in (b) exhibits a shift in the Ni $2p_{3/2}$ and Ni $2p_{1/2}$ peaks to a higher BE. The oxidation state of Ni atoms assessed from the BE of Ni $2p_{3/2}$ (855.8 eV) and Ni $2p_{1/2}$ (873.2 eV) was found to be 2+, corresponding to $Ni(OH)_2$. Besides this, a small amount of NiO is also present with its corresponding Ni $2p_{3/2}$ peak at 853.8 eV and Ni $2p_{1/2}$ peak at 871.3 eV). The presence of NiO could be mainly caused by dehydration of $Ni(OH)_2$. Figure 3.10 (c) shows the XPS spectrum of the charged sample with a mechanical etching of 0.1mm. It is observed that the mechanically etched sample exhibits Ni $2p_{3/2}$ and Ni $2p_{1/2}$ peaks for multiple phases of nickel such as Ni^0 (red), NiO (yellow), and $Ni(OH)_2$ (blue), where the majority phase belongs to $Ni(OH)_2$. Furthermore, the center of gravity of these peaks lies in between the peak positions of Ni^0 and $Ni(OH)_2$. This indicates that the electrolyte can penetrate through 0.1 mm thickness of the sample and can participate in the charge storage process. The charged electrode was further mechanically etched by 0.2 mm and it's corresponding XPS spectrum is shown in Figure 3.10 (d). As seen, the sample exhibits a majority phase of Ni^0 rather than $Ni(OH)_2$. The center of gravity of Ni $2p_{3/2}$ and Ni $2p_{1/2}$ peaks are closer to Ni^0.Therefore, by observing the positions of Ni $2p_{3/2}$ and Ni $2p_{1/2}$ peaks

at different depths in the charged samples, respective ionic states of nickel were determined. It is then estimated that about 0.2 mm of the outer surface of the electrode participates in the charge-discharge measurements. The mass of this layer was used further for calculating the specific capacitance of the material.

Table 3.1. Amount of nickel in nickel nanoparticle impregnated carbonized wood samples.

Concentration of Nickel nitrate	% of Ni
0.5 M	5.5 %
1 M	14.8 %
2 M	20.4 %
3 M	27.5 %

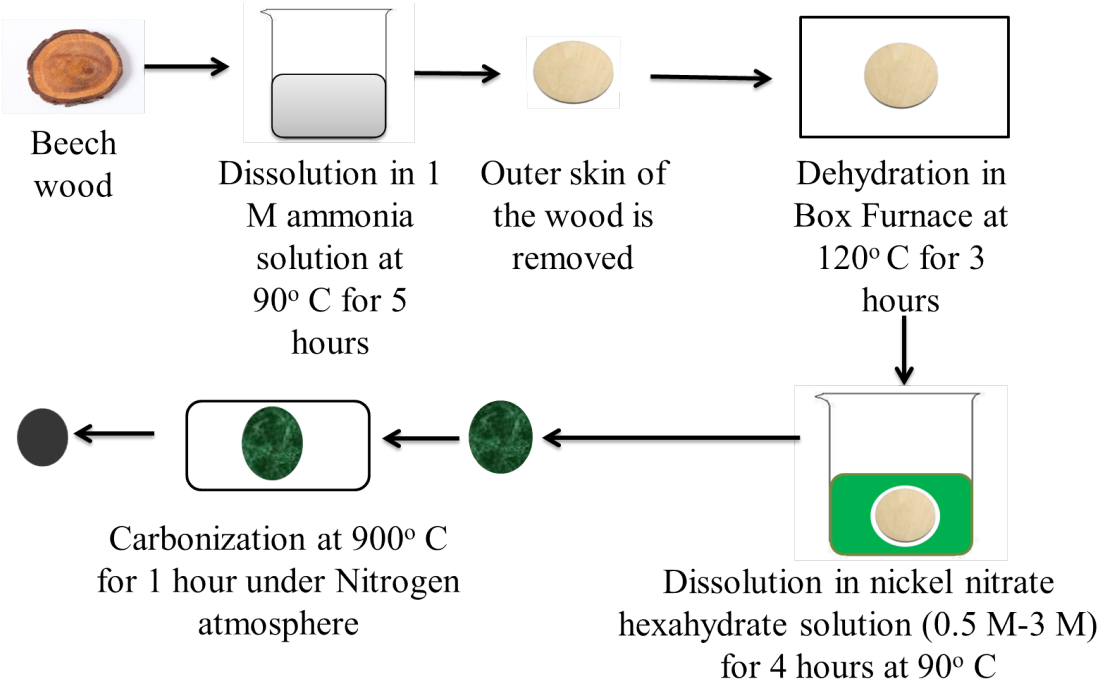

Figure 3.1. Schematic diagram of the preparation of nickel nanoparticle impregnated carbonized wood samples.

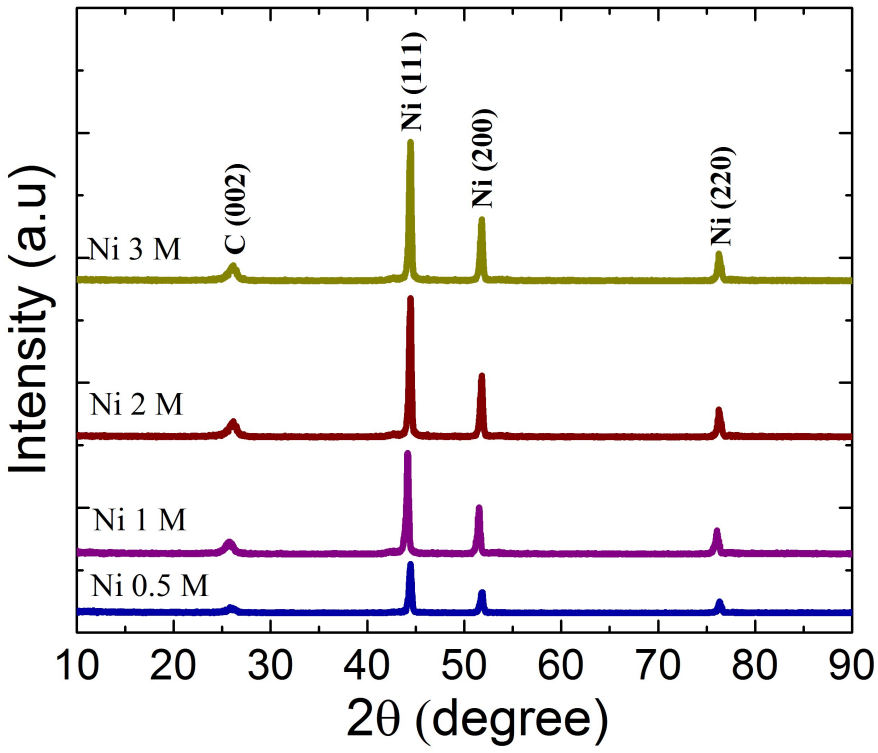

Figure 3.2. XRD spectra of Nickel nanoparticle impregnated in carbonized wood.

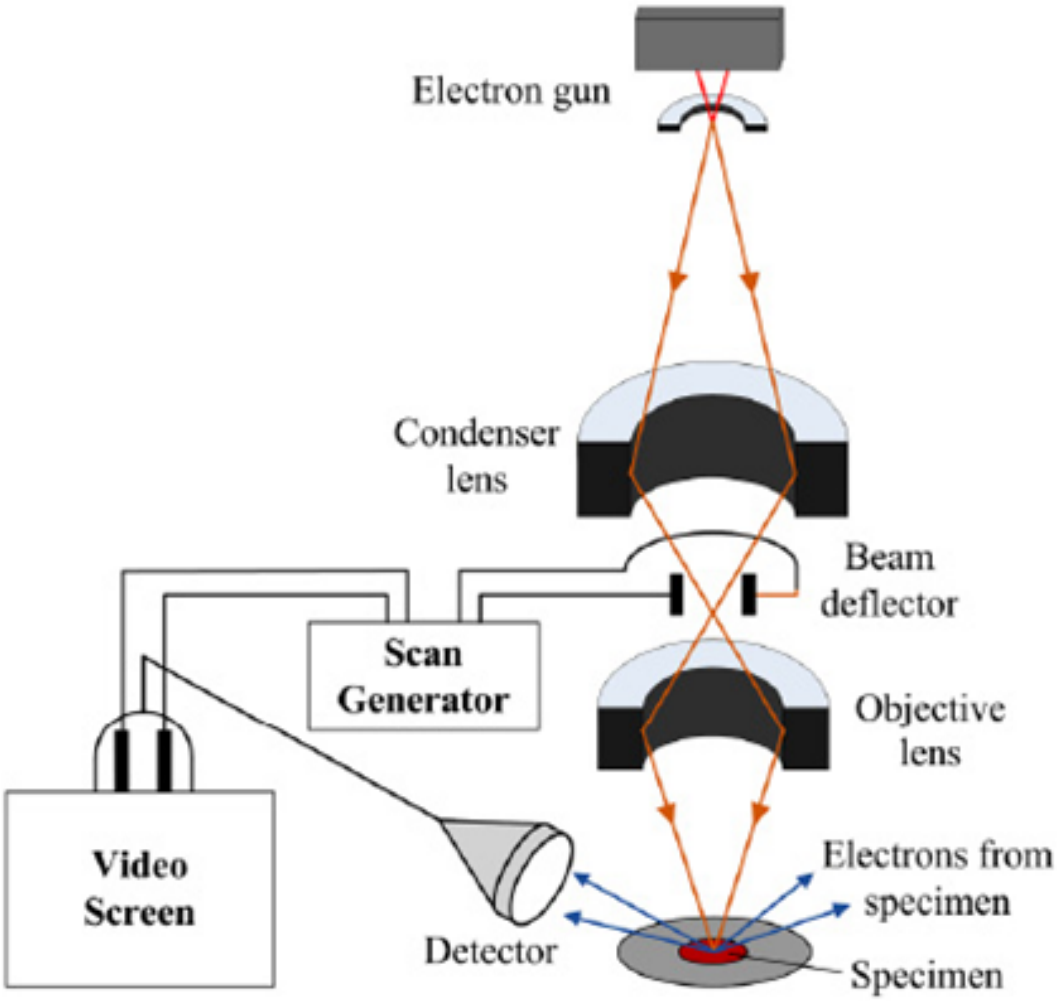

Figure 3.3. Schematic illustration of working principle of Scanning Electron Microscopy (SEM) (37).

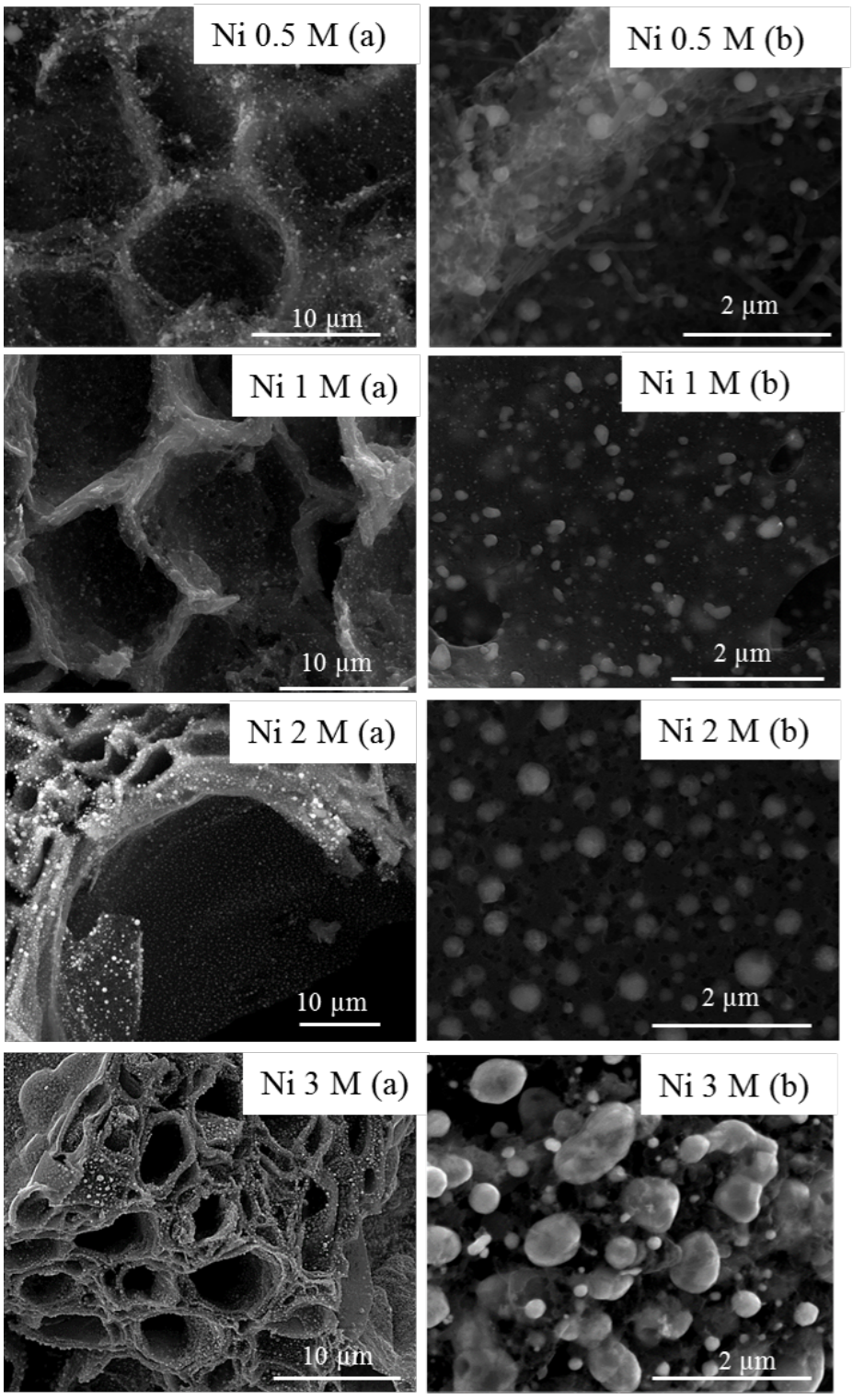

Figure 3.4. SEM images at (a) low magnification, (b) high magnification for Ni 0.5 M, Ni 1 M, Ni 2 M, and Ni 3 M.

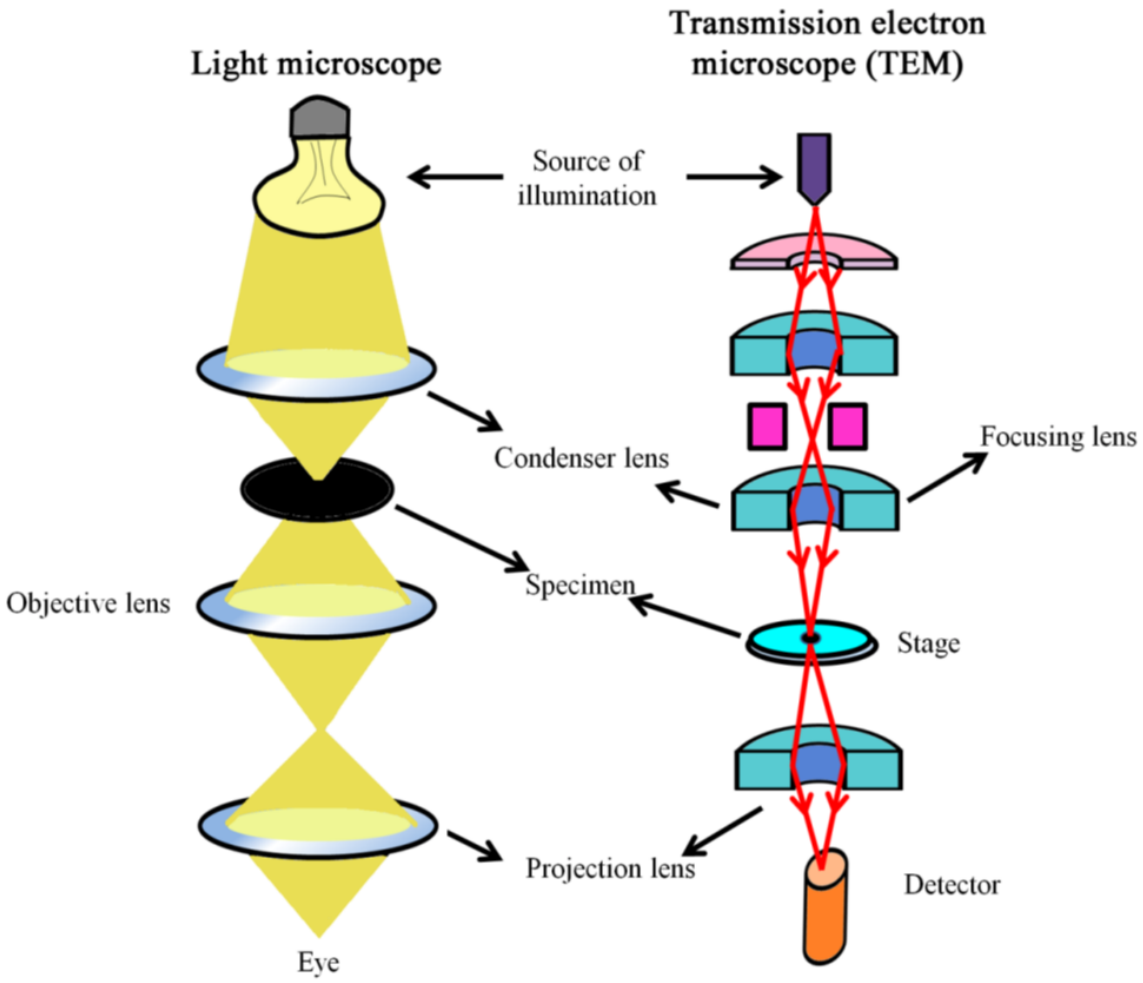

Figure 3.5. Schematic illustration of the working principle of Transmission Electron Microscopy (TEM) (37).

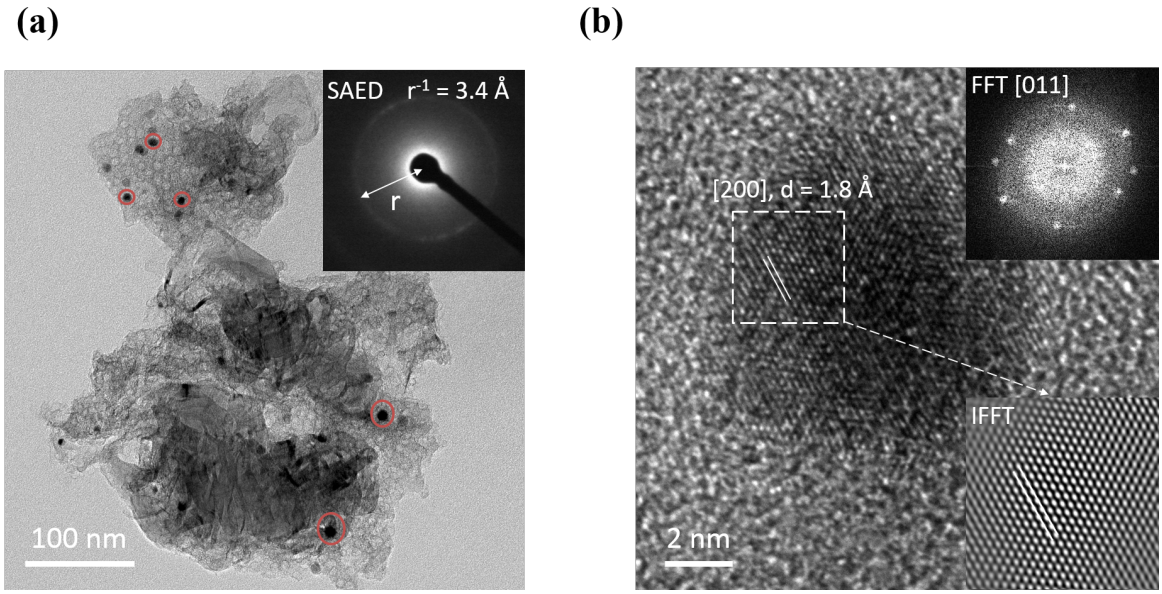

Figure 3.6. TEM images at (a) low resolution, (b) high resolution for nickel nanoparticle impregnated carbonized wood.

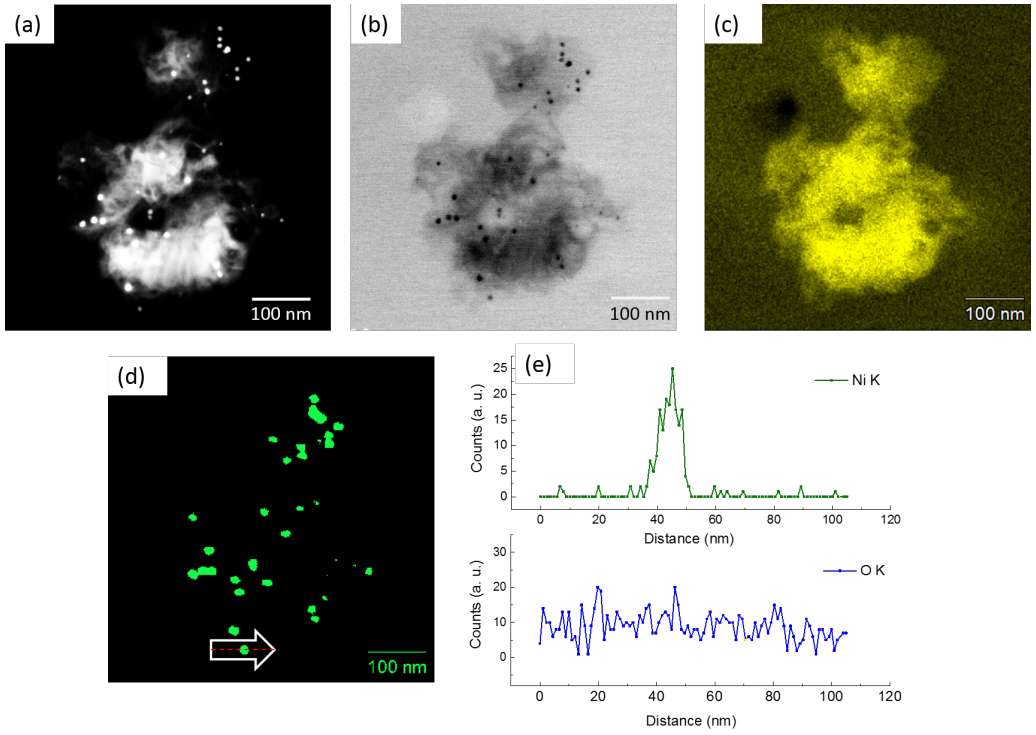

Figure 3.7. TEM images at (a) bright field, (b) dark field, (c) distribution of carbon, (d) distribution of nickel, (e) line profile of nickel and oxygen across the nickel nanoparticle for nickel nanoparticle impregnated carbonized wood.

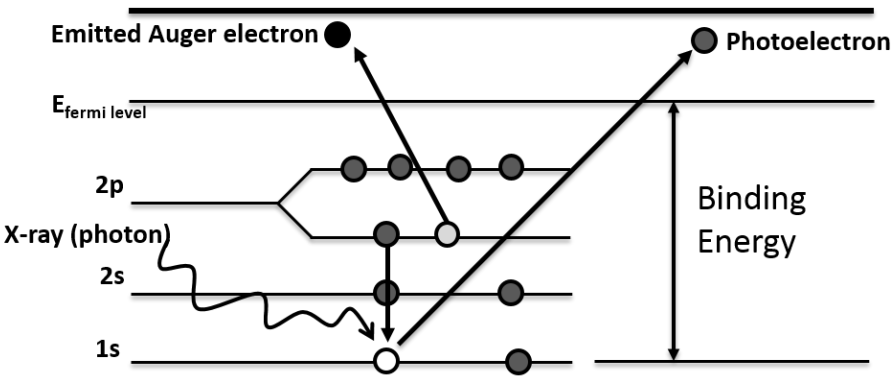

Figure 3.8. Schematic diagram showing the working principle of X-ray photoelectron spectroscopy.

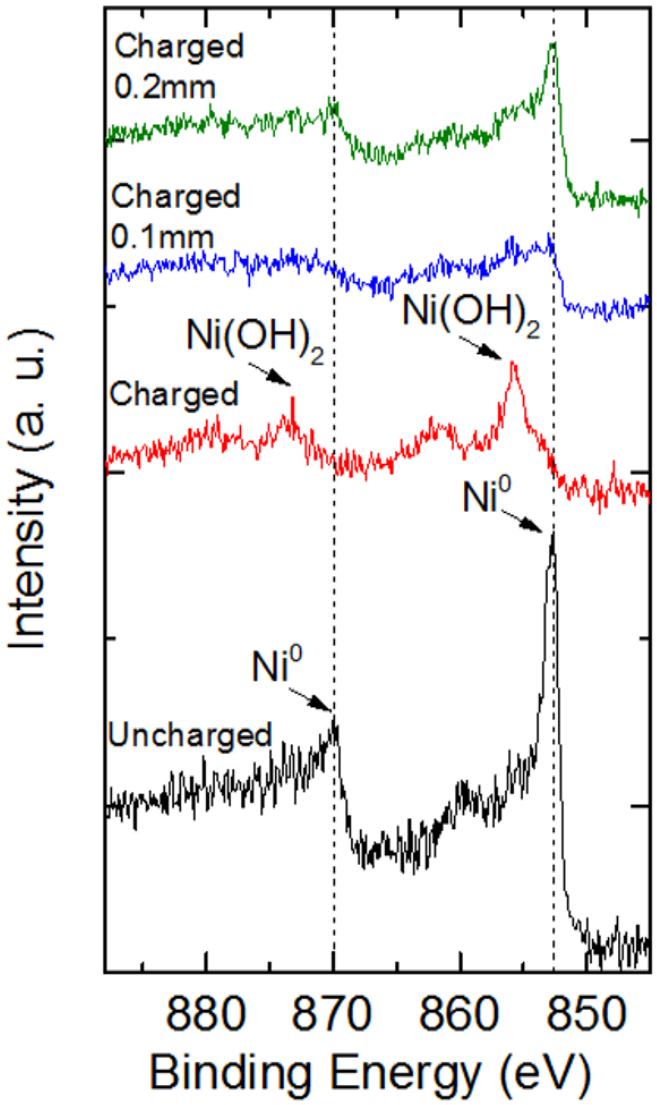

Figure 3.9. High-resolution XPS scans for uncharged, charged and charged with successive mechanical etching samples of nickel nanoparticle impregnated carbonized wood.

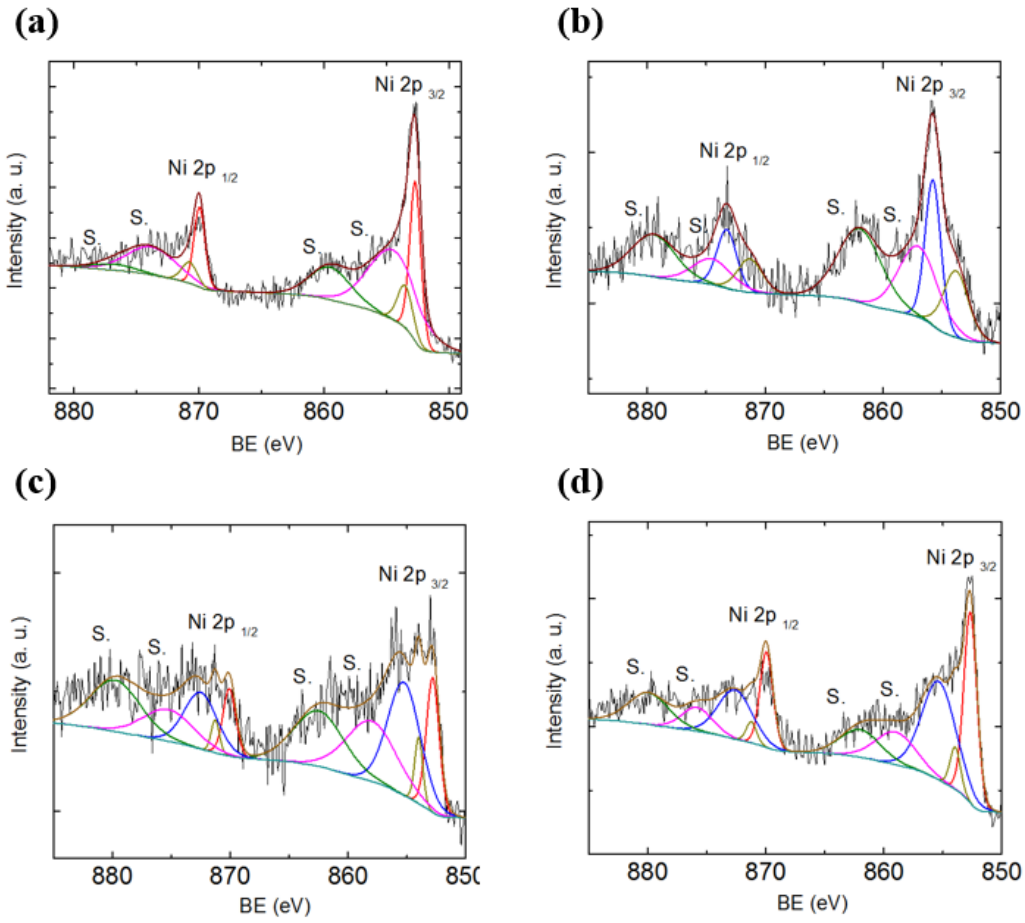

Figure 3.10. Resolved fitting of XPS spectrum for (a) uncharged sample, (b) charged sample, (c) charged sample with mechanical etching of 0.1 mm, (d) charged sample with mechanical etching of 0.2 mm. The satellite peaks are indicated by S. Nickel metallic phase, that is, Ni^0 is indicated by red, nickel oxide (NiO) is indicated by yellow, and $Ni(OH)_2$ is indicated by blue.

CHAPTER 4

ELECTROCHEMICAL CHARACTERIZATION OF NICKEL/CARBON-BASED COMPOSITE ELECTRODES

To test the nickel nanoparticle impregnated carbonized wood electrode as a supercapacitor, a three-electrode electrochemical cell is utilized with nickel nanoparticle impregnated carbonized wood electrode is used as the working electrode, platinum sheet as the counter electrode, and Ag/AgCl as a reference electrode. A 5 M KOH solution is used as an electrolyte. A Gamry Potentiostat reference 600^{TM} is used for electrochemical testing. The complete setup is shown in Figure 4.1.

4.1 Cyclic Voltammetry

The Cyclic Voltammetry (CV) technique is a potentiodynamic process in which a known potential is applied to the working electrode and the current response is measured. The applied potential is changed as a function of time. The rate of change of potential with time is known as the scan rate and its units are given by V/s. Depending on the scan rate, the time for which the experiment progresses could be estimated. In a typical CV experiment, the potential is ramped up from the initial voltage to the voltage limit and is then later scanned back.

During the forward scan as the voltage increases from a lower potential to the voltage limit, the measured current response also increases. However after reaching the voltage limit the scan reverses its direction. During this backward scan, the voltage decreases and the current response changes, resulting in a CV plot. The total charge that is accumulated at the electrode surface could be found by integrating the measured current with respect to time. In other words, the integrated area of the CV curve would give the total volumetric charge (38). With the help of the integrated area, one can estimate the capacitance of the working electrode as shown in the following derivation.

Consider the CV curve shown Figure 4.2 (a) at different scan rates varying from 1 mV/s to 10 mV/s. Let us denote the area for 1 mV/s scan rate under the charge curve (0 V-0.5 V) as A1 and that of the area under the discharge curve (0.5 V - 0 V) as A2, k ($\frac{\delta V}{\delta t}$) as the scan rate where δV is the voltage window, and δt is the time. The capacitance obtained from charging and discharging are considered to be equal. From Equation 1.1 we know that

$$C = \frac{Q}{V} \tag{4.1}$$

$$C = \frac{I \times \delta V \times \delta t}{\delta V} \tag{4.2}$$

$$C = \frac{I \times \delta V}{\frac{\delta V}{\delta t}} \tag{4.3}$$

$$C = \frac{I \times \delta V}{k} \tag{4.4}$$

$$C \times k = I \times V \tag{4.5}$$

$$C \times k \times \partial V = I \times V \times \partial V \tag{4.6}$$

$$\int_{0V(V1)}^{0.5V(V2)} C \times k \times \partial V = \int_{0V(V1)}^{0.5V(V2)} I \times V \times \partial V = -A1 \tag{4.7}$$

Therefore,

$$C \times k \times (V2 - V1) = A1 \tag{4.8}$$

$$C \times k \times (V1 - V2) = A2 \tag{4.9}$$

Subtracting equation 4.8 from 4.9 we get

$$2C \times k \times (V1 - V2) = A1 - A2 \tag{4.10}$$

Therefore,

$$C = \frac{A1 - A2}{2k(V1 - V2)} \tag{4.11}$$

Besides the capacitance, the shape of the CV curve of a supercapacitor is typically used to study electrochemical properties of the electrode such as the redox reactions, electron transfer kinetics, and optimising the potential window of the electrode. For instance, a reversible reaction, if occurring in a working electrode, could be easily recognized by observing the shape of a CV curve. In other words, reduction and oxidation reactions occurring could be observed from the forward and backward scans, which is related to the oxidation or reduction potentials. Furthermore, at these potentials, a hump or a peak in the CV curve could be observed. A reduction reaction is usually observed by a decrease in

the peak potential and is called a cathodic peak, whereas an oxidation reaction is observed with an increase in the peak potential, which is typically called an anodic peak. The anodic and cathodic peak correspond to the positive and negative currents, respectively.

Typically, a CV curve plays an important role in supercapacitors as it helps in understanding the difference between an ideal supercapacitor and a supercapacitor influenced by a psuedocapacitance. A rectangular-shaped CV plot with no peaks corresponds to an ideal capacitor commonly known as EDLCs, whereas a CV plot in wave form with peaks indicates the influence of psuedocapacitance arising due to the redox or faradic reactions. Commonly, three or more scans are used in studying the behavior of the sample. Although the first scan of a CV shows the peaks, the full data or the analysis can be obtained from the subsequent scans as the system takes time to stabilize to the surrounding environment.

Apart from knowing the redox reactions, it is highly important to understand the shape of a CV curve. Two common effects are normally used in explaining the shape (12,39). They are (a) Equilibrium effect given by Nernst equation, which describes that the reduction/oxidation at the electrode surface does not occur until the initial potential at the surface of the electrode reaches the reduction/oxidation potential; (b) Transport effect, which describes the influence of diffusion of ions on the limitation of current determined by rate of transport. This limitation in current could be explained by the potential across the electrode surface, that is, the larger the potential at the electrode surface, the more the depletion of the electrode near to the electrolyte.

A typical CV curve for a supercapacitor, for example, if we consider nickel nanoparticle impregnated carbonized wood electrodes, is shown in Figure 4.2. If one could observe clearly at every scan rate, the reduction current decreases with a decrease in the potential further, that is, even after the reduction reaction has occured. This is because the electrolyte depletes near to the electrode surface and starts to diffuse, thereby creating a diffusive layer as seen in Chapter 2. Therefore, the current depends on the rate at which the ions from the electrolyte can diffuse to the surface of the electrode. Furthermore, the diffusion kinetics could also help in understanding the decrease in the current. According to the diffusion kinetics, when no potential is applied to the electrode, the concentration is same across the electrode and given by the bulk concentration. When the potential is ramped up/changed, the electrode surface reaches the reduction potential at some point. As a result, as more and more reduction occurs the depletion at the electrode surface increases, resulting in more diffusion of ions. Therefore, the size of the diffusive layer increases. This increase in the diffusion can be understood from Fick's first law of diffusion which is given by

$$J = \frac{\partial C}{\partial t} = D\frac{\partial C}{\partial X} \tag{4.12}$$

where $\frac{\partial C}{\partial t}$ is the rate of change in the concentration and $\frac{\partial C}{\partial X}$ is the change in concentration with respect to the distance from the electrode surface. Therefore, as the distance of the diffusive layer changes with time, the rate of change in the concentration changes, thereby diminishing the current across the surface. Hence, once the reduction peak potential has passed, the rate of diffusion of ions from the electrolyte to the electrode surface keeps going slower and therefore there is a decrease in the current. However, this decrease in the current never reaches zero in a CV curve. This is due to the nonfaradic currents which arise when the movement of the charge and ions are indistinguishable. Furthermore, the nonfaradic currents result in a charge accumulation at the electrode surface. The amount of charge accumulation is proportional to the potential of the electrode which creates current at the surface.

For a fixed potential window, CV curves are also affected by scan rates. As seen in Figure 4.2, at a lower scan rate, the magnitude of the current is smaller when compared to the higher scan rates. This is because, at a lower scan rate, the diffusive layer can enlarge further apart from the electrode (as the time taken to record a CV is longer), thereby resulting in a smaller amount of flux ($\frac{\partial C}{\partial t}$) being generated.

$$i = nFAJ \tag{4.13}$$

Since we know the amount of current is proportional to the flux at the electrode according to Equation 4.13, where 'i' is the current, 'n' is the number of electrons, 'F' is Faraday's constant, 'A' area of the electrode surface, 'J' is the flux at the electrode surface therefore at a lower scan rate, the magnitude of the current response to the applied potential is smaller. However, at a higher scan rates, the size of the diffusive layer is smaller, which increases the magnitude of the current response.

Figure 4.2 (a-d) and 4.3 (a-d) illustrates the CV behavior of the nickel nanoparticle impregnated carbonized wood electrode with varying concentrations of nickel content. During the CV experiment, the voltage range was set from 0 V - 0.5 V and the scan rates used ranged from 1 mV/s to 50 mV/s. Figure 4.2 (a-d) represents the CV curve at low scan rates (1 mV/s to 10 mV/s) and Figure 4.3 (a-d) represents the CV curves at high scan rates (25 mV/s to 50 mV/s). We can observe from Figure 4.2 that all the curves are not rectangular in shape, unlike that of pure carbonized wood shown in Figure 4.4, but instead are in a wave form, which reveals the capacitive characteristics of the nickel

nanoparticles impregnated carbonized wood electrode (40). Furthermore, a distinct pair of redox peaks is observed during forward (anodic) and backward (cathodic) scans, indicating the pseudocapacitive behaviour of the electrode arising due to the charging process and discharging process.The charging process is when the nickel is oxidized to nickel hydroxide, while the subsequent discharging process is when the nickel hydroxide is reduced back to nickel. This charging and discharging process follows the following redox reaction (41-44): $Ni + 2OH^- \leftrightarrow \alpha - Ni(OH)_2 + 2e^-$.

Interestingly, with the increase in the scan rate from 1 mV/s to 10 mV/s the shape of the CV curve remains unchanged except for the increase in the anodic peak potential and the decrease in the cathodic peak potential as observed in Figure 4.2. Additionally, there is an increase in the separation distance between the anodic peak potential and the cathodic peak potential as seen in Figure 4.5, indicating a good electrochemical reversibility. Furthermore, the anodic peak current and the cathodic peak current values are proportional to the square root of the scan rate as illustrated in Figure 4.6, indicating that the reaction is reversible and is limited by the diffusion of the ions (45). It can be observed from Figure 4.2, that the area of the CV curve increases from Ni 0.5 M to Ni 2 M, implying that the specific capacitance increases with the increase in the concentration of nickel. This may be attributed to the presence of nickel nanoparticles, which increase the surface area and further enhance the pseudocapacitance, resulting in the increase of overall capacitance of the electrode. However, the area of the CV curve for Ni 3 M is less than the Ni 0.5 M, Ni 1 M, and Ni 2 M, indicating that the specific capacitance decreases after the nickel concentration is increased to above 2 M. This decrease in the specific capacitance can be due to the decrease in the relative mass of the active materials (nickel nanoparticles) (45).

4.2 Electrochemical Impedance Spectroscopy

In order to utilize electrochemical supercapacitors as power devices, the electrode should have a low resistance to achieve high capacitance value and to minimize the power losses. The AC impedance technique, that is, Electrochemical Impedance Spectroscopy (EIS) measurements, are employed to quantitatively determine the relative resistance values of the electrode, electrolyte and their interface. EIS is used to study the dynamics of an electrochemical process. It is mainly used to characterize the electrochemical process in terms of electrical measurements. In an EIS technique, electrochemical impedance is measured by applying a small amplitude of AC voltage and thereby measuring the current throughout the cell. The frequency of the AC signal is changed throughout the measurements, thus

giving out an impedance value at each of the frequencies. The range of impedance values is plotted against frequency values and the output gives either a Bode plot or a Nyquist plot. Bode Plot has the log frequency as X-axis with the absolute value of total impedance and phase shift on the Y-axis. By using a bode plot one can know the impedance value at any particular frequency. However, the Nyquist plot has a real part and an imaginary part of impedance, which are plotted against each other as X-axis and Y-axis, respectively. Each point on the Nyquist plot gives the impedance at one frequency (39).

EIS data are analysed by using an equivalent electrical circuit model where one tries to find a model which matches to the impedance from the measured data. Some of the typical circuit elements used in the model are the resistors, capacitors, and inductors. These elements are to be used such that they have a basis in physical chemistry or electrochemistry. For example, the resistor is used to characterize the solution's resistance in the electrochemical cell along with the resistance of electrode. Table 4.1 shows the common circuit elements with their equation for their current v/s voltage and impedance. It can be seen from Table 4.1 that the resistor is independent of frequency, although the inductor and the capacitor depend on the frequency. As the frequency increases, the impedance also varies. Using an equivalent circuit model, one can know the electrolyte resistance, double-layer capacitance, charge transfer resistance, and the diffusion coefficient. The elements used in the equivalent circuit models with their corresponding impedance and admittance are shown in Table 4.2.

In the present study, we use a mixed control circuit model with kinetic and charge transfer control in which the polarization in the electrochemical cell is due to the combination of kinetic and diffusion processes. This can be modeled as the double layer capacitance (C_{dl}), which is connected in parallel to the charge transfer resistance (R_{ct}). Due to the diffusion of ions playing a major role, a further element called the Warburg impedance W is added in series to the R_{ct}. The R_{ct} arises mainly due to the difference in the conductivity at the electrode and electrolyte. In addition to these elements, there is a combinational resistance at the electrolyte interface which is given by R_e. The impedance measurements are carried out at a frequency range between 10^6 Hz and 0.1 Hz. Figure 4.7 (a), (b) show the Nyquist plots of nickel nanoparticle impregnated carbonized wood electrodes and pure carbonized wood with a potential amplitude of 0.1 V, respectively. A simple circuit model to evaluate the Nyquist plot is shown in Figure 4.8.

In order to determine the R_{ct} and the equivalent series resistance, the Nyquist plot has been correlated to the mixed control circuit model. The complex impedance plot (Nyquist plot) shows a depressed semicircle corresponding to a high-frequency region which

is attributed to the charge transfer phenomenon in the system due to the Faradic reactions. The diameter of the depressed semicircle arc gives the charge transfer resistance. From the fitting, the R_{ct} obtained for the nickel nanoparticle impregnated carbonized wood samples showed similar consistency with the increase in the nickel concentration and was found to be approximately equal to 0.13 Ohms. Furthermore, at the high-frequency region, the curve first meets the X-axis and gives the equivalent series resistance of the electrode (ESR). Figure 4.7 (b) shows the EIS plot of pure carbonized wood. It was found that the ESR of the nickel nanoparticle impregnated carbonized wood samples (1.97 Ohms, 2.19 Ohms, 2.27 Ohms, and 2.37 Ohms for Ni 0.5 M,Ni 1 M,Ni 2 M, and Ni 3 M respectively) was less than the pure carbonized wood (2.9 Ohms), implying that the presence of nickel nanoparticles in the carbonized wood helps in improving the conductivity of the electrode. At a lower frequency, the EIS plot is almost linear, which corresponds to the Warburg diffusion, W, and is described as the diffusive resistance of the OH^{-1} ions within the pores of the nickel nanoparticle impregnated carbonized wood electrode.

4.3 Galvanostatic Charge-Discharge

In order to understand the charging and discharging behaviour of the electrode, a galvanostatic charge-discharge technique is employed. For a galvanostatic charge-discharge method, a constant current is applied and the output voltage v/s time is plotted. In this technique, the supercapacitor is charged from the initial voltage to a preset voltage. Once it has reached the preset voltage, the supercapacitor discharges till it reaches the initial voltage. The output data, that is, voltage v/s time is plotted for both the charge and discharge. The difference in the voltage between the point where the charging ends and the discharge starts gives the iR drop or the potential drop. The iR drop occurs due to a high internal resistance or the equivalent series resistance. A high internal resistance can be due to the high conductivity of the electrolyte and bad geometry of the electrode. The iR drop can be reduced by varying the concentration of the electrolyte according to the different electrochemical systems.

One of the characteristic terms used to define a supercapacitor is specific capacitance. This can be calculated using the discharge time and is given by Equation 4.14, where ‘i’ is the current, ‘m’ is the mass of the electrode material participating in charge-storage process as determined by XPS, ‘dt’ is the discharge time, and ‘dv’ is the voltage window.

$$C_s = \frac{i \times dt}{m \times dV} \tag{4.14}$$

In the present study we conducted the galvanostatic charge-discharge experiments for the nickel nanoparticle impregnated carbonized wood electrodes at various current densities ranging from 8 A/g to 120 A/g with a potential voltage range of 0 V - 0.5 V. Figure 4.9 represents the Charge-discharge curves for nickel nanoparticle impregnated carbonized wood samples with varying nickel concentration. Additionally, the charge-discharge measurements were also performed for pure carbonized wood under identical conditions. Results are shown in Figure 4.10. As seen from Figure 4.9 and 4.10, the discharge time decreases with the increase in the current density. This is because, with the increase in the current density, the input current increases and the time that is taken either to charge or to discharge the supercapacitor is smaller, which thereby limits the number of accessible pores within the electrode. In other words, as the current density increases, the charging and the discharging are limited only to the outer layers of the porous electrode. It is also observed that the charging and discharging curves are nonlinear, with changes in the slope being observed for nickel nanoparticle impregnated carbonized wood. This change in the slope is due to the reaction between the electrolyte ions and the nickel nanoparticle impregnated carbonized wood electrode. The change in slope in the charge-discharge curves implies that the electrode is consuming the charge through the anodic reaction and is later discharging by the cathodic reaction, indicating that the charge transformation is reversible. Furthermore, the changes in the slopes match with the peak potentials of the CV curve as seen in Figure 4.2. In addition to the redox pairs of peaks, the nonlinear charge-discharge curve proves that the nickel nanoparticle impregnated carbonized wood electrodes exhibit a psuedocapacitive behaviour.

The specific capacitance for all the nickel nanoparticle impregnated carbonized wood samples for various nickel concentrations at different current densities is calculated using Equation 4.14. Figure 4.11 represents the specific capacitance for all the nickel nanoparticle impregnated carbonized wood electrodes at various current densities. As seen from Figure 4.11, the specific capacitance increases with the increase in the concentration of nickel nitrate content up to 2 M, beyond which the specific capacitance decreases. A highest specific capacitance of about 3616 F/g was obtained for Ni 2 M sample. This is higher than the amorphous $Ni(OH)_2$ (1544 F/g), porous NiO film (188 F/g), graphene sheets/NiO film (324 F/g), hierarchically porous graphene $Ni(OH)_2$ (hGN) hybrid hydrogel (600 F/g), $Ni(OH)_2$/graphene/Ni foam (1600 F/g), $Ni(OH)_2$/CNT/Nickel Foam (3300 F/g), $Ni(OH)_2$/Ni/graphene nanocomposite (2609 F/g) (47-54).

At 40 A/g of current density, a specific capacitance of 2884 F/g, 3037 F/g, 3328 F/g, and 1440 F/g were obtained for Ni 0.5 M, Ni 1 M, Ni 2 M, and Ni 3 M respectively. Additionally,

it is observed that at all the current densities the specific capacitance of Ni 2 M are higher than Ni 0.5 M and Ni 1 M. This is because as the amount of nickel concentration increases the contribution of the psuedocapacitance due to the nickel on the overall capacitance increases. Additionally, the nickel nanoparticles are uniformly distributed throughout the surface, which leads to a higher specific surface area. Besides this, the nickel nanoparticles impart surface polarity to the electrode and increase the capacitance due to the dipole affinity of OH^- ions towards the electrode (55). In contrast, the Ni 3 M sample showed a lower specific capacitance than Ni 0.5 M, Ni 1 M, and Ni 2 M at all current densities, as seen in Figure 4.11. This can be attributed to the presence of larger particle size of nickel nanoparticles. Furthermore, the nickel nanoparticles are closer to each other when compared to other samples. Therefore, during the charging-discharging process the nickel nanoparticles aggregate together, thereby reducing the surface area and the accessibility of pores towards the electrolyte.

However, for a supercapacitor to be used for fast charge-discharge applications, it should show a high specific capacitance even at higher current density. In other words, the supercapacitor should have a high rate capability. It was observed that the Ni 2 M sample exhibited a specific capacitance of 2245 F/g even at 120 A/g current density, which proves that the nickel nanoparticle impregnated carbonized wood samples can also undergo the redox reaction at a higher current density as well.

In addition to this, galvanostatic charge-discharge experiments were employed to understand the behaviour of charge discharge of a pure carbonized wood sample and is shown in Figure 4.10. Specific capacitance is calculated using equation 4.14 and was found to be 136 F/g, which is less than the nickel nanoparticle impregnated carbonized wood samples. This proves that by the addition of nickel nanoparticles into the wood, the conductivity and the specific capacitance show a tremendous increase, which implies that the nickel nanoparticle impregnated carbonized wood has a potential to be utilized as an electrode for supercapacitors.

4.4 Energy Density and Power Density

As already mentioned in Chapter 1, the major drawback of a supercapacitor is its low energy and power density. In this study, to improve the energy and power density of a supercapacitor, we tested nickel nanoparticle impregnated carbonized wood as an electrode for a supercapacitor. The energy density and power density at various current densities for the nickel nanoparticle impregnated carbonized wood samples are calculated using Equation

4.15 and 4.16, respectively, where 'C_s' is the specific capacitance which is obtained from the charge-discharge curves, 'V' is the voltage window and 't' is the discharge time in seconds obtained from the charge-discharge data.

$$\text{Energy Density } (E) = \frac{1 \times CV^2}{2 \times 3.6} \tag{4.15}$$

$$\text{Power Density } (P) = \frac{(3600 \times E)}{t} \tag{4.16}$$

Figure 4.12 represents the Ragone plot, that is. the log-log plot of Power density (W/kg) v/s the energy density (Wh/kg) for nickel nanoparticle impregnated carbonized wood samples at various current densities. From Figure 4.12 it can be comprehended that a power density of as high as 30 kW/kg is obtained for Ni 2M at 120 A/gm current density. Additionally, Ni 3 M, Ni 1 M, and Ni 0.5 M samples exhibited similar power density of about 30 kW/Kg respectively.

Besides power density, supercapacitors are also characterized by their energy density. An energy density of 125.6 Wh/kg is obtained for Ni 2M sample at 8 A/gm current density, calculated from equation 4.15. This proves that the nickel nanoparticle impregnated carbonized wood electrodes have a good energy density when compared to other composite materials.

4.5 Cyclic Life Test

In order to utilize a supercapacitor for practical purposes, a cyclic life test is performed wherein the galvanostatic charge-discharge experiments are repeated for a long term and at a defined scan rate. The units of the scan rate used in this experiment are given by A/gm, that is, current density. The capacitance retention between the first cycle to the known cycle (for example 500^{th} cycle) is thus calculated. In this study, the cyclic life test experiment is conducted for nickel nanoparticle impregnated carbonized wood electrodes for 6000 cycles at a scan rate of 40 A/gm over a voltage range of 0 V-0.5 V.

Figure 4.13 represents the cyclic life test of the nickel nanoparticle impregnated carbonized wood samples which are plotted between the specific capacitance retention and cycle number. From Figure 4.13, it can be seen that Ni 3 M retains a capacitance of about 87% in the initial 500 cycles and decreases further thereafter. After 6000 cycles, Ni 3 M sample finally retains about 62% of its initial capacitance. This poor stability of the Ni 3M can be due to large volume changes during the charge-discharge occurring due to the insertion and removal of the electrolyte ions in the porous structure. Despite this, its specific capacitance after 6000 cycles is still higher than that of pure carbonized wood.

In contrast to Ni 3 M sample, Ni 2 M, Ni 1 M, and Ni 0.5 M samples undergo a slow decay in their specific capacitance for their initial 500 cycles and continues to decay upto 6000 cycles. For example, Ni 2 M retains a specific capacitance of 98% after 500 cycles and finally about 89% after 6000 cycles. Similarly, Ni 1 M retains a specific capacitance of 97% after 500 cycles and later about 84% after 6000 cycles. Likewise, Ni 0.5 M retains a specific capacitance of 94% after 500 cycles and 82% after 6000 cycles. In other words, Ni 2 M, Ni 1 M, and Ni 0.5 M retain a specific capacitance of greater than 80% after 6000 cycles of repeated charge-discharge experiments. This excellent stability of capacitance retention proves that the nickel nanoparticle impregnated carbonized wood electrodes have an excellent potential as electrodes for supercapacitors.

Table 4.1. Common electrical elements and their response.

Component	Current vs voltage	Impedance
Resistor	$E = iR$	$Z = R$
Inductor	$E = Ldi/dt$	$Z = j\omega L$
Capacitor	$I = CdE/dt$	$Z = 1/j\omega C$

Table 4.2. Circuit elements used in equivalent circuit model.

Equivalent element	Admittance	Impedance
R	$\frac{1}{R}$	R
C	$j\omega C$	$\frac{1}{j\omega C}$
L	$\frac{1}{j\omega L}$	$j\omega L$
W (Infinite Warburg)	$Y_o\sqrt{j\omega}$	$\frac{1}{Y_o\sqrt{j}}$
O (Finite Warburg)	$\frac{1}{Y_o\sqrt{(j\coth(B\sqrt{j}))}}$	$\frac{\tanh((B\sqrt{j})}{(Y_o\sqrt{j}))}$
Q (CPE)	$Y_o(j)^\alpha$	$\frac{1}{Y_o(j)^\alpha}$

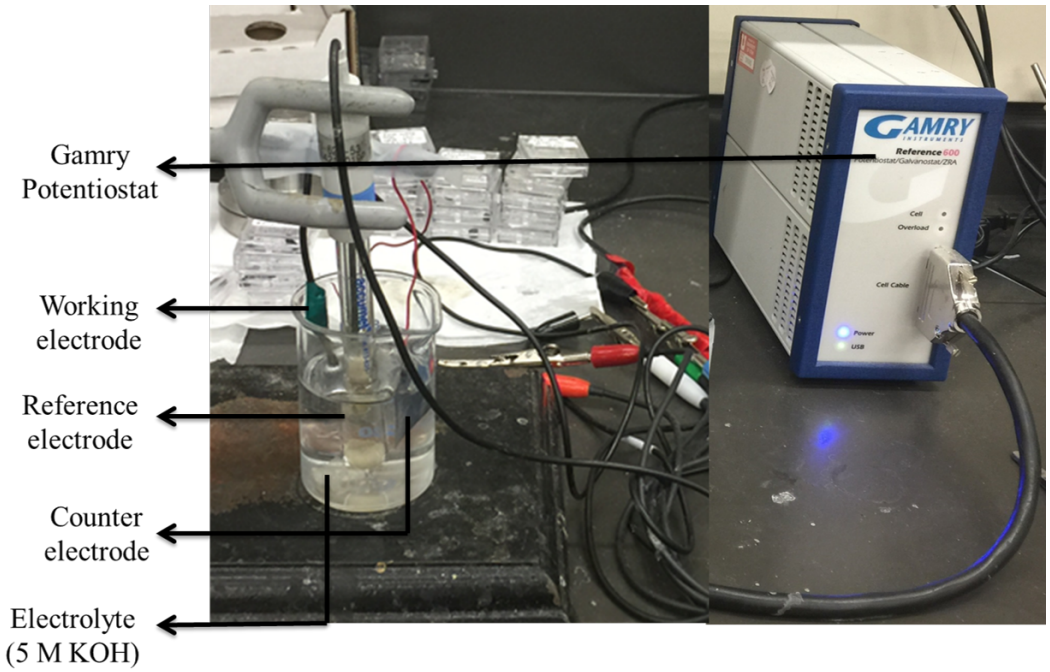

Figure 4.1. Schematic diagram of three electrode electrochemical cell setup connected to the Gamry Potentiostat. The working electrode is nickel impregnated carbonized wood, counter electrode is Platinum sheet, and the reference electrode is Ag/AgCl.

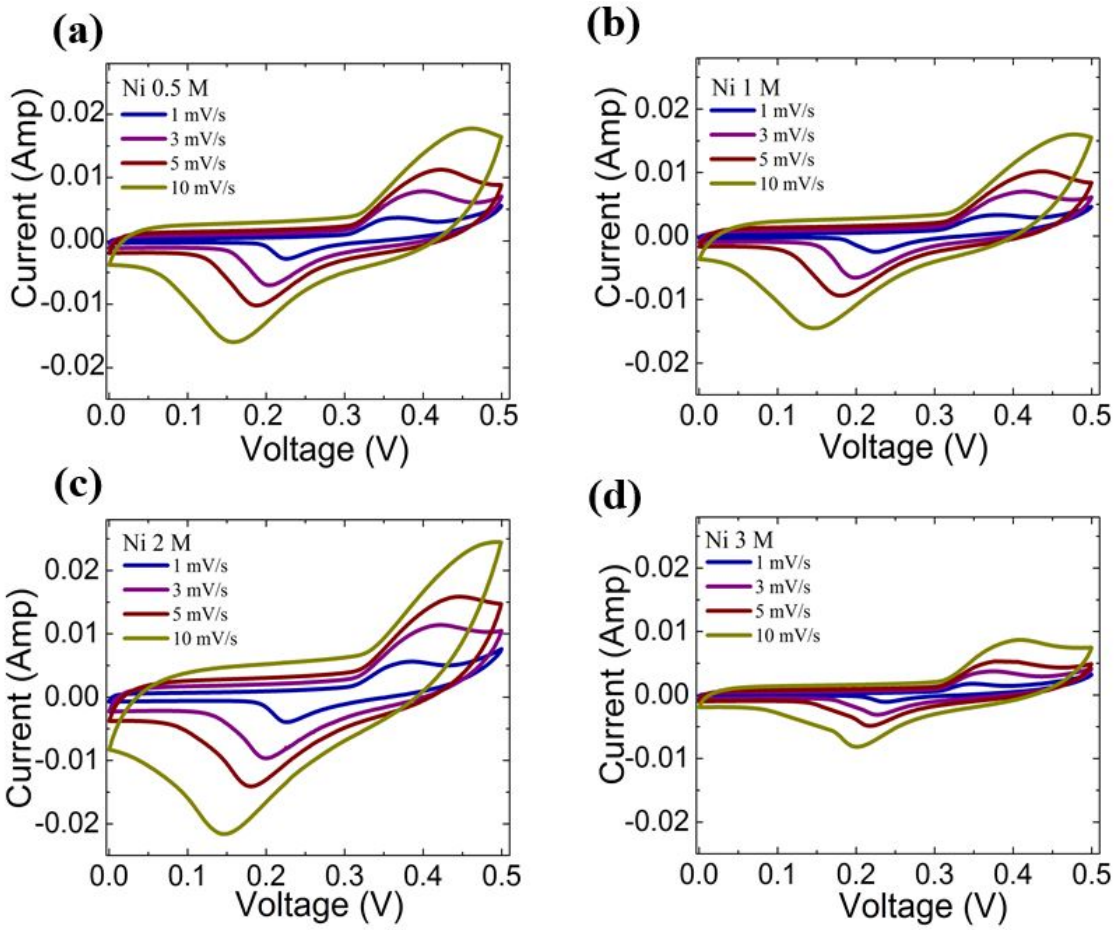

Figure 4.2. Cyclic Voltammetry plots of (a) Ni 0.5 M, (b) Ni 1 M, (c) Ni 2 M, and (d) Ni 3 M at scan rates varying from 1 mV/s to 10 mV/s.

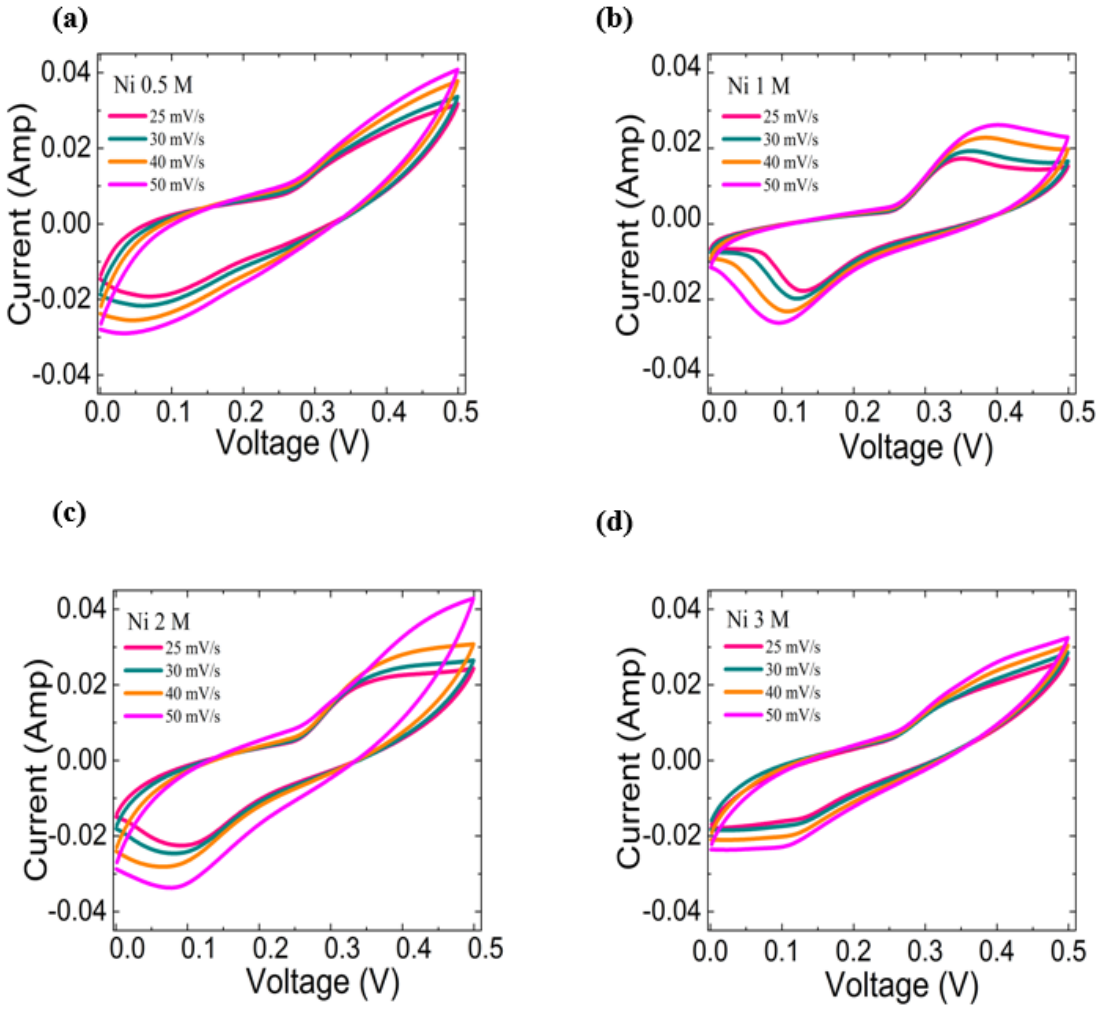

Figure 4.3. Cyclic Voltammetry plots of (a) Ni 0.5 M, (b) Ni 1 M, (c) Ni 2 M, and (d) Ni 3 M at scan rates varying from 25 mV/s to 50 mV/s.

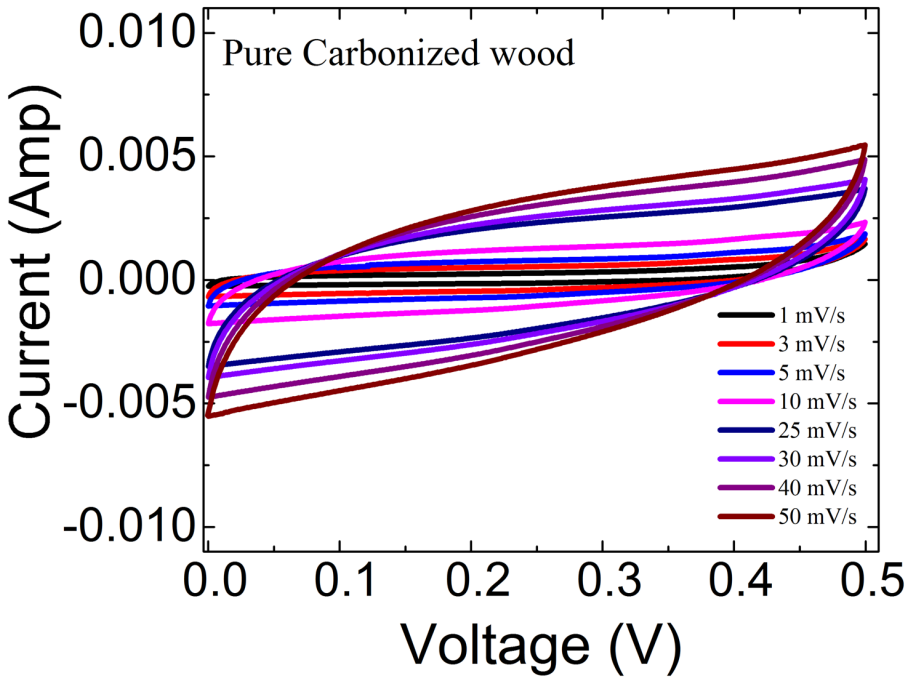

Figure 4.4. Cyclic Voltammetry plots of pure carbonized wood at varying scan rates.

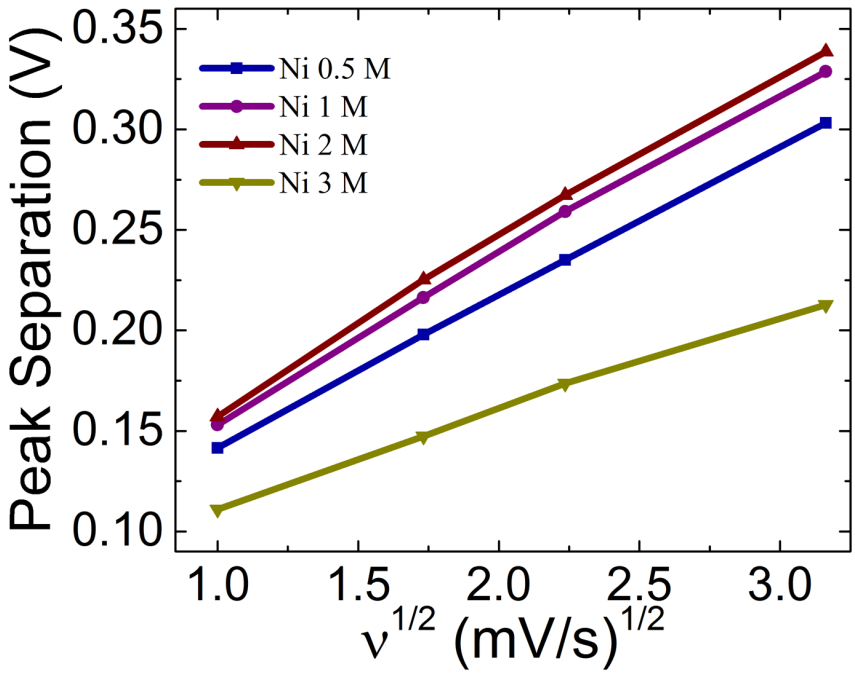

Figure 4.5. Peak separation v/s square root of scan rate for Ni 0.5 M, Ni 1 M, Ni 2 M, and Ni 3 M.

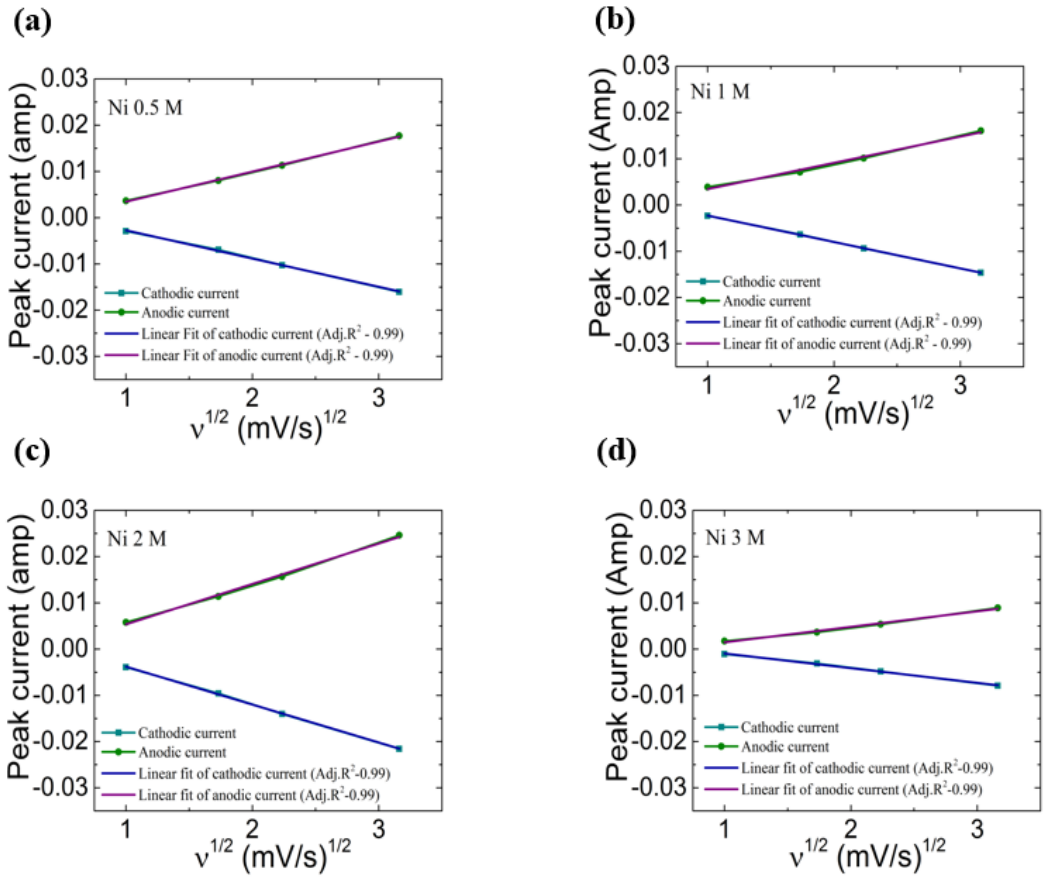

Figure 4.6. Peak current v/s square root of scan rate for Ni 0.5 M, Ni 1 M, Ni 2 M and Ni 3 M indicating the process is diffusion controlled.

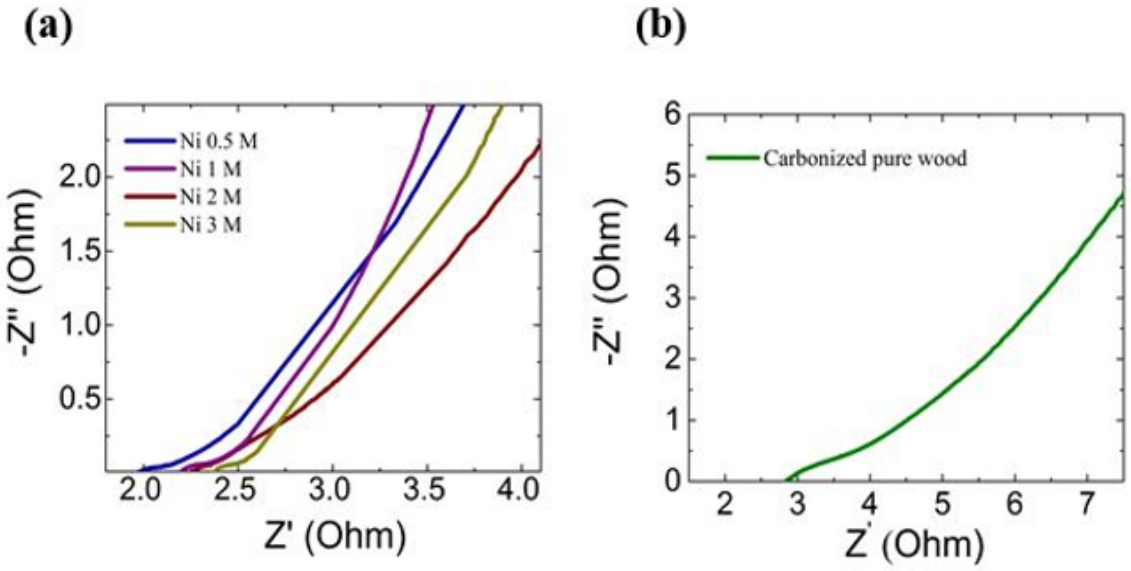

Figure 4.7. (a) Nyquist Plots of Ni 0.5 M, Ni 1 M, Ni 2 M, and Ni 3 M, (b) pure carbonized wood at frequency range from 10^6 Hz to 0.1 Hz with an applied AC voltage of 0.1 V.

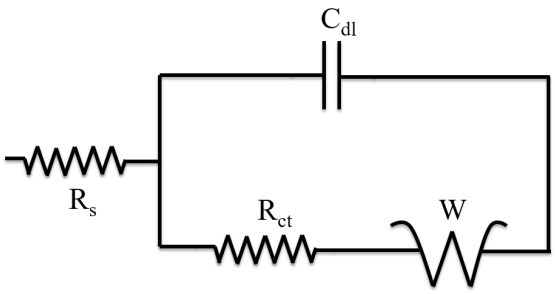

Figure 4.8. Schematic diagram of mixed control circuit used for evaluating Nyquist plots.

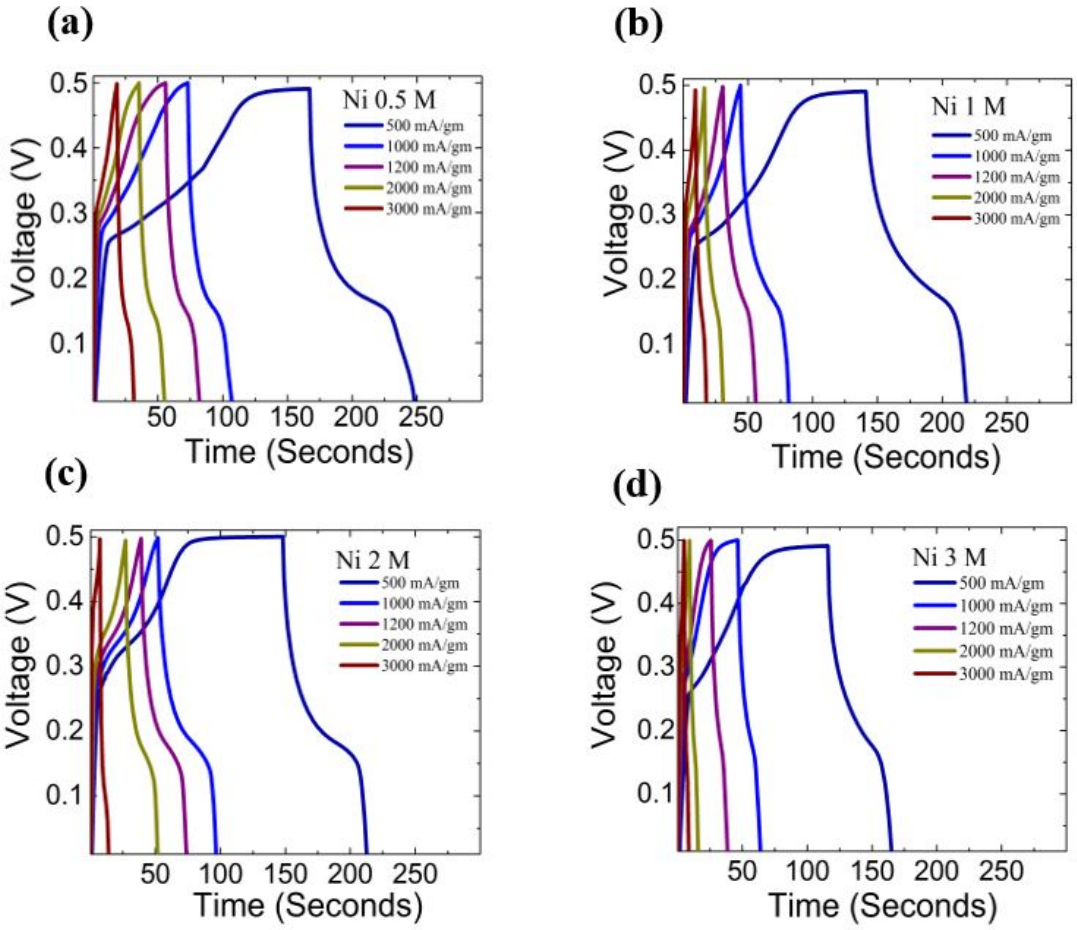

Figure 4.9. Galvanostatic charge-discharge curves for (a) Ni 0.5 M, (b) Ni 1 M, (c) Ni 2 M, and (d) Ni 3 M at current densities ranging from 8 A/g to 120 A/g.

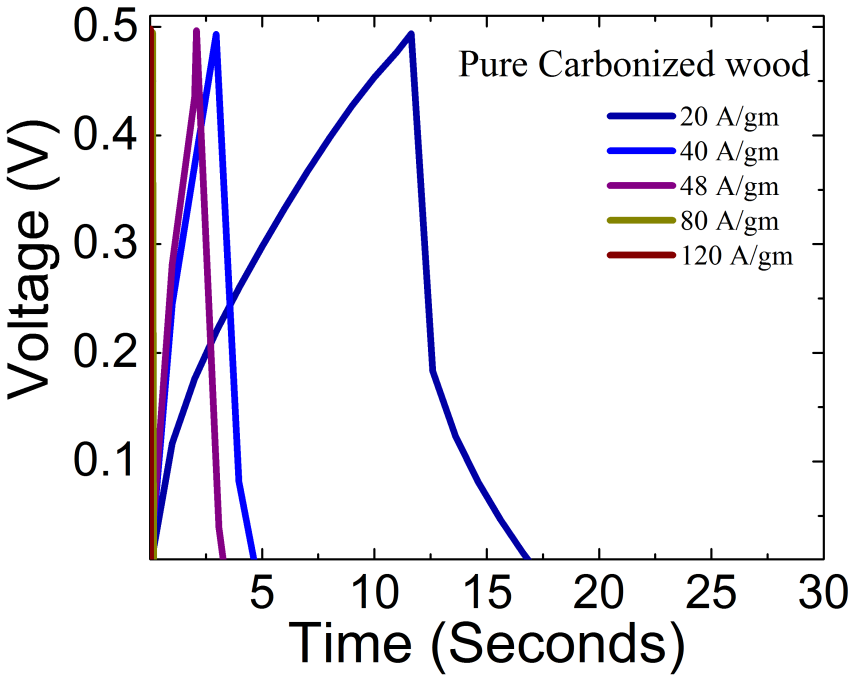

Figure 4.10. Galvanostatic charge-discharge curves for pure carbonized wood at current densities ranging from 8 A/g to 120 A/g.

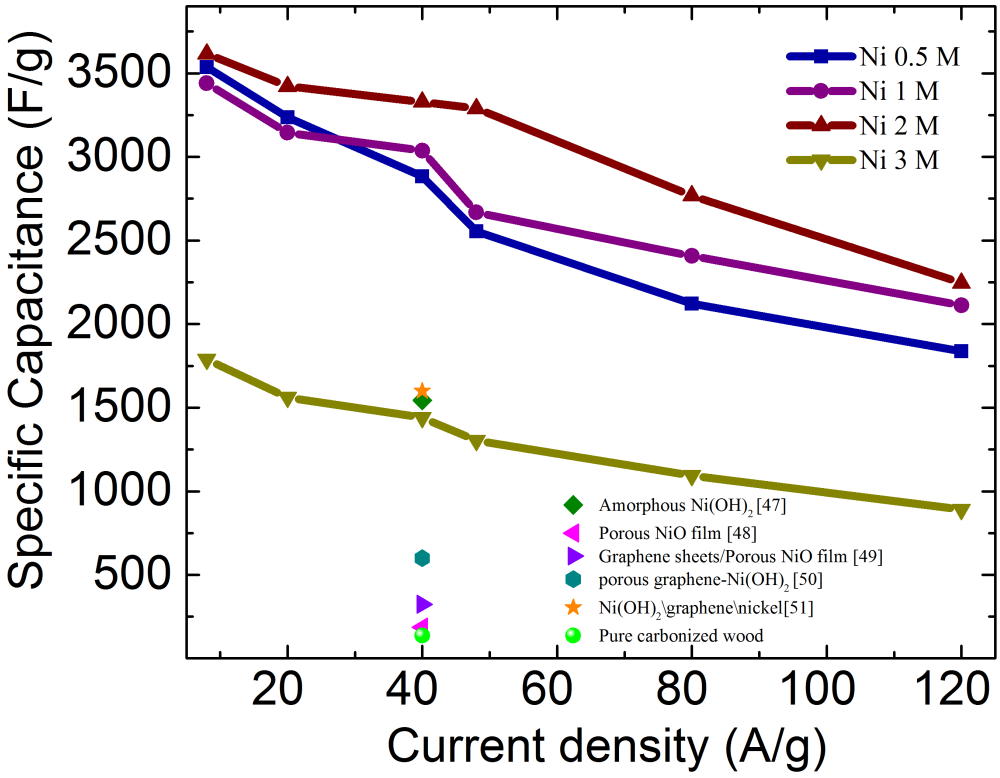

Figure 4.11. Relationship between current density and specific capacitance for Ni 0.5 M, Ni 1 M, Ni 2 M, and Ni 3 M. Also includes specific capacitance of various electrodes at 40 A/g current density.

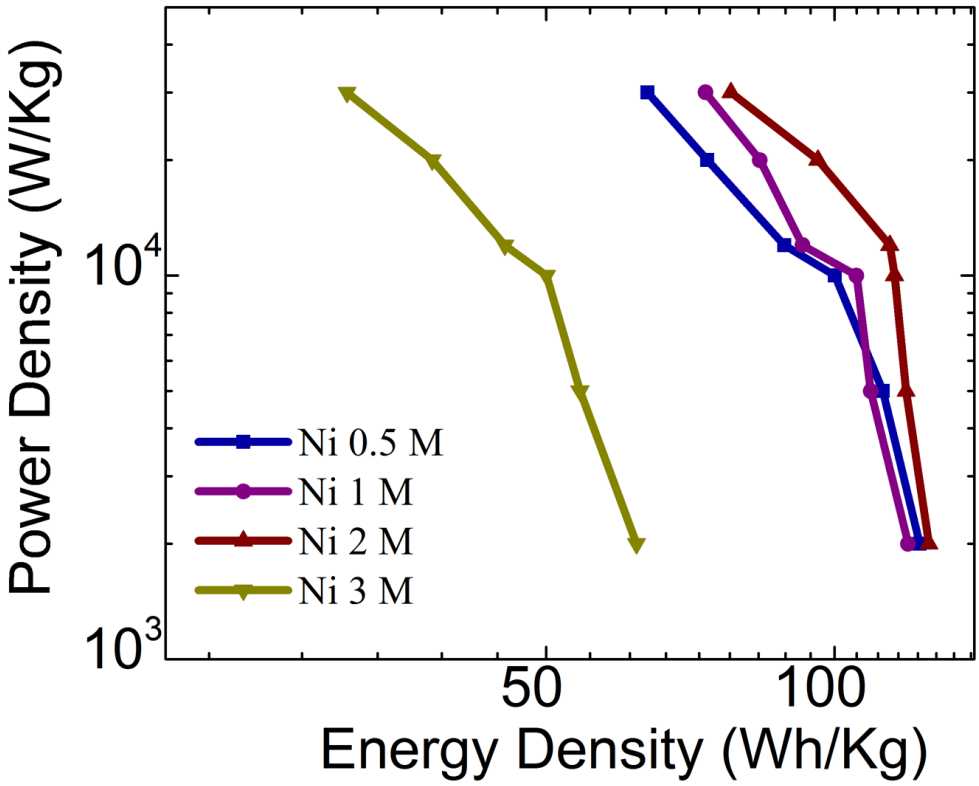

Figure 4.12. Ragone plot showing the energy density and power density at various current densities for Ni 0.5 M, Ni 1 M, Ni 2 M, and Ni 3 M.

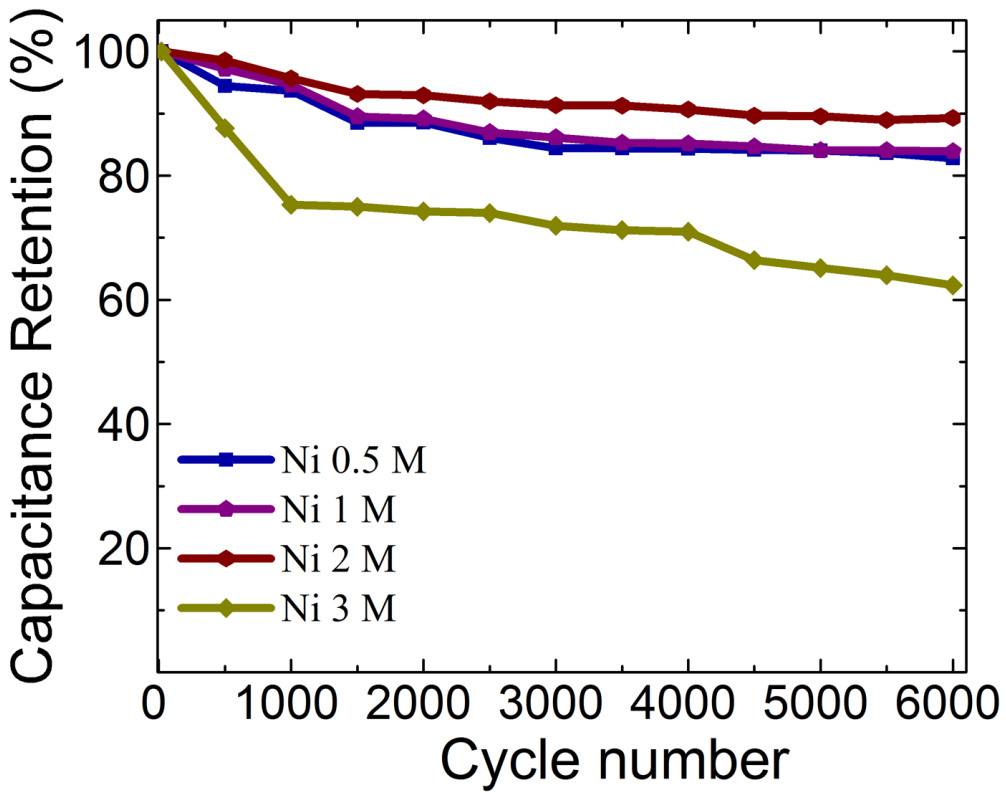

Figure 4.13. Cyclic life test for Ni 0.5 M, Ni 1 M, Ni 2 M, and Ni 3 M conducted at 40 A/g current density.

CHAPTER 5

CONCLUSION AND FUTURE WORK

As discussed in Chapters 3 and 4, herewith a brief summary of the results is presented. This chapter also provides an outlook for future work. The future work mainly discusses the improvement of carbon structure by modifying the synthesis process and also the possible potential psuedocapacitive materials for supercapacitor applications.

5.1 Summary

Nickel nanoparticles in varying concentrations are naturally impregnated into carbonized wood, which is further used for practical applications, mainly as supercapacitors. When compared to other metal oxides and metal composites, nickel nanoparticle impregnated carbonized wood have several advantages, including a low cost of fabrication. In order to utilize the nickel nanoparticle impregnated carbonized wood samples as electrode materials for supercapacitors, electrochemical measurements such as Cyclic Voltammetry, Electrochemical Impedance Spectroscopy, and galvanostatic charge-discharge experiments were performed. The Cyclic Voltammetry of the nickel nanoparticle impregnated carbonized wood samples exhibited a pair of peaks which indicate the redox reaction occurring between Ni to Ni^{+2}. This shape of the CV curve with peaks indicates the presence of psuedocapacitive behavior of nickel nanoparticle impregnated carbonized wood electrode. This is further supported by the nonlinear charge-discharge curves which are obtained from the galvanostatic charge-discharge experiments. From the galvanostatic charge-discharge experiments, the key characteristics of a supercapacitor, that is, specific capacitance, power density, and energy density are calculated. It is observed that the specific capacitance increases with the increase in the nickel concentration from 0.5 M to 2 M. However, after an increase in the concentration of nickel from 2 M to 3 M the specific capacitance has decreased, thus suggesting that the 2 M concentration is the optimal amount present in the carbonized wood. A specific capacitance of as high as 3616 F/g at 8 A/g current density is obtained for Ni 2 M, which is higher than amorphous $Ni(OH)_2$ (1544 F/g), porous NiO film (188 F/g),

graphene sheets/NiO film (324 F/g), hierarchically porous grapheneNi$(OH)_2$ (hGN) hybrid hydrogel (600 F/g), Ni$(OH)_2$/graphene/Ni foam (1600 F/g), Ni$(OH)_2$/CNT/Nickel Foam (3300 F/g), Ni$(OH)_2$/Ni/graphene nanocomposite (2609 F/g), and pure carbonized wood (136 F/g). In addition to this, the Ni 2M sample exhibits a power density of 750 W/kg and an energy density of 125.6 Wh/kg. Furthermore, in order to practically use the nickel nanoparticle impregnated carbonized wood electrodes as a supercapacitor, cyclic life test is performed. Ni 2 M showed outstanding capacitance retention of about 80% after 6000 cycles of charge-discharge. These excellent results indicate that nickel nanoparticle impregnated carbonized wood can be used for practical applications such as supercapacitors.

5.2 Future Work

Despite of the fact that this thesis has demonstrated the potential of nickel nanoparticle impregnated carbonized wood as an electrode for supercapacitor applications, several prospects for extending the scope of the thesis remain. This section presents some of the future directions.

- **Improving the form of carbon in the electrode matrix**: As mentioned in Chapters 2 and 3, carbon acts as a supporting material in the electrode matrix. Furthermore, it is highly conductive and can act as a source of electron-transfer catalyst. Moreover, a high surface area of carbon increases the double-layer capacitance, thereby increasing the overall capacitance of the material. Improving the carbon from graphitic phase to carbon nanostructures such as carbon nanotubes could enhance the performance of the supercapacitors. Carbon nanotubes provide an excellent combination of high porosity and low resistance. Low electrode resistance reduces the power losses and a high porosity helps in charge-transfer and diffusion of ions from the electrolyte. Therefore, a careful synthesis process has to be designed to obtain carbon nanotubes from wood by optimizing the activation and carbonization temperatures.

- **Improving the energy density and power density by adding different psuedocapacitive elements**: Apart from naturally impregnating nickel nanoparticles into carbonized wood as a source of psuedocapacitance, future studies on the influence of co-impregnation of copper nanoparticles, manganese nanoparticles, and ruthenium oxide nanoparticles to nickel nanoparticles has to be studied. Apart from the transition metals, composites of Nickel-Nickel oxide (Ni-NiO) nanoparticles, Copper-Copper oxide (Cu-CuO) nanoparticles, and Manganese-Manganese oxide (Mn-MnO_2) nanoparticles

impregnated in the carbonized wood could also be investigated as an electrode material for supercapacitors.

APPENDIX A

ENERGY HARVESTING IN OXIDE-BASED THERMOELECTRIC MATERIALS

Apart from energy storage, this thesis also aims to give a prospective idea about energy generation using Thermoelectric materials which are bio-compatible and stable at high temperatures. Thermoelectric materials (TE) can be utilized for dual roles. Firstly, they can convert the waste heat into electricity based on the underlying Seebeck effect. Secondly, heat can be transferred from one side of the device to the other under an external electric field, based on the Peltier effect. In the former case, the TE materials have a potential to be utilized in cold conditions to produce heat, whereas in the latter case they can be utilized for refrigeration or for cooling. TE generators possess a vast scalability and are capable of having a long life span of reliable operation. Most of the TE devices utilizing the Seebeck effect and Peltier effect can be found in various applications such as transport vehicles, microelectronics, wine coolers, space science and cooling, remote wireless sensors such as networks, biomedical devices, wrist watches, radioactive thermal generators, and many more (56-60).

The conversion efficiency of TE materials is given by a dimensionless quantity figure of merit, which depends on the intrinsic properties of the material. The figure of merit ZT is given by $S^2T/\rho\kappa$, where S, ρ, κ, and T are the Seebeck coefficient, electrical resistivity, thermal conductivity, and absolute temperature, respectively. In order to use any TE material for practical purposes, the figure of merit (ZT) should be at least greater than one (ZT $>$ 1). Although there are materials such as tellurium-based, antimony-based, and germanium-based compounds whose figure of merit is greater than 1, they are limited in their applications due to their chemical stability and toxicity (61). Furthermore, at high temperatures these materials degrade/evaporate, limiting their application to low working temperatures. Therefore, there is a need to have TE materials which are not limited to their working temperature, chemically stable, nontoxic, and have a high figure of merit.

Keeping in mind these requirements, much research is focused on the development

of metal oxides as TE materials for high temperatures due to their thermal robustness and chemical stability, than heavy alloys. Furthermore, these oxide-based materials are non-toxic, corrosion resistance which are greater and can be abundantly found, unlike the tellurium- and antimony-based alloys, and possess facile synthesis techniques. Research on oxide-based materials was initially overlooked due to its insulating-like behaviour, low electrical conductivity, and low atomic mass relative to other TE materials. Moreover, they have a high atomic vibration frequency and thermal conductivity. However, in order to obtain a high figure of merit, the TE material should possess a high electrical conductivity and low thermal conductivity. A low resistivity is needed to reduce the joule heating, and a low thermal conductivity is required to maintain a high temperature gradient between the hot and cold ends of the TE device so as to obtain a higher Seebeck voltage.

Research on oxide-based TE materials came to light when the first layered cobalt-oxide-based ceramic $Na_2Co_2O_4$ was reported by Teraski et al. who demonstrated that the synthesized layered cobalt-oxide-based ceramic, that is, $Na_2Co_2O_4$ exhibited a high Seebeck coefficient of 100 μ/K with a low electrical resistivity of 200 μ.cm at 300 K (62). However, sodium being hygroscopic in nature and volatile above 800^oC limits its use in practical applications. Therefore, much research was focused on the development of other layered cobalt oxides (63-67). Although there was tremendous research on the development of oxide-based ceramics, $Ca_3Co_4O_9$ gained lots of prominence due to its high chemical and thermal stability at high temperatures.

In 2003, Shikano et al. synthesized single crystals of $Ca_3Co_4O_9$ whose figure of merit was nearly 0.87 at 973 K (68). Nevertheless, due to small grain size, single crystals of $Ca_3Co_4O_9$ were limited to practical applications. Recent investigations have been focused on the development of novel TE metal oxides by modifying the crystal structure in order to control the electron and phonon transport separately, and thus enhancing the figure of merit. One of the methods to control the electron and phonon transport separately is by synthesizing polycrystalline materials that possess a complex crystal structure.

$Ca_3Co_4O_9$ is composed of two layers of alternate stacking of a conductive CdI_2-type hexagonal CoO_2 layer with 2-dimensional triangular lattice and a block layer composed of insulating rock salt (RS) structure as shown in Figure A.1. A structural misfit exists along the b-axis between the two sublattices as they have an identical a, c, and β but different b parameters. The CdI_2-type hexagonal CoO_2 layer with 2-dimensional triangular lattices of Co-ions is formed by edge sharing of CoO_2 octahedra. The Co ions which are edge shared in the CdI_2 type hexagonal CoO_2 layer dominate the carrier transport and determine the

electronic properties of $Ca_3Co_4O_9$. There are two types of Co ions, Co^{3+} and Co^{4+}, present in this sublattice. The hopping of majority charge carriers in the material, that is, holes between Co^{3+} and Co^{4+} states along the lattice sites cause the electrical conductivity of $Ca_3Co_4O_9$. The RS structure contains only one type of Co ions (Co^{2+}). These (Co^{2+}) ions are considered charge reservoirs which supply the holes to the CdI_2 type hexagonal (Co^{2+}) layer. Furthermore, the sublattice reduces the mean free path and decreases the thermal conductivity of the material, which results in a higher figure of merit.

A polycrystalline $Ca_3Co_4O_9$ can be synthesized by various techniques, which include the traditional solid state synthesis, sol-gel processing, spark plasma sintering, polymer solution method, and so forth. Although a polycrystalline state is achieved by these methods, the electrical resistivity obtained is higher. As a result, the figure of merit or the conversion efficiency is low.

There are different ways in which one can improve the figure of merit utilizing the polycrystalline samples. One way is to synthesize the polycrystalline material by ionic substitution, improving the synthesis process, or by doping another material. The addition of doping can result in decrease in the carrier scattering at the grain boundaries, and thereby decreases the electrical resistivity. For instance, M. Pervel et al. investigated the effect of doping rare earth elements such as Pr, Nd, Eu, Dy, and Yb in a $Ca_3Co_4O_9$ system and observed that substitution of trivalent ion for Ca^{2+} decreases the hole concentration and thereby increases the Seebeck coefficient and electrical resistivity (69). Y. Wang et al. studied the effect of substitution of univalent ions, that is, Ag^{+}, in a $Ca_3Co_4O_9$ system and showed a decrease in the electrical resistivity and increase in Seebeck coefficient simultaneously with an increase in the figure of merit. This enhancement is due to the improvement of charge carrier concentration and change in carrier mobility (70). Apart from univalent and trivalent substitutions, studies on divalent substitution for Ca^{2+} have also been investigated. Recently, G. Constantinescu studied the effect of doping small amounts of Mg^{2+} for Ca^{2+} in a $Ca_3Co_4O_9$ system. In his study, it was observed that the addition of small amounts of Mg^{2+} decreases the RS layer size which results in an increase in the Seebeck coefficient. Furthermore, the electrical resistivity decreased upon increasing the magnesium content due to the variations in the charge carrier concentration. As a result, addition of Mg^{2+} resulted in an increase in the power factor when compared to undoped $Ca_3Co_4O_9$ (71).

Basing on the idea of doping, we have substituted heavy ion, that is, terbium in Tb^{3+} and Tb^{4+} states for Ca^{2+} in $Ca_3Co_4O_9$ and studied its effect on microstructure, thermal transport properties such as the Seebeck coefficient, electrical resistivity, thermal conduc-

tivity, power factor, and figure of merit. These studies were performed using a home-made setup. Samples ($Ca_{3-x}Tb_xCo_4O_9$) of more than 50 in number were synthesized with doping concentration (x) varying from 0 to 0.9 using the solid state synthesis technique. Subsequent X-ray diffraction measurements performed on these samples showed a homogeneous phase of $Ca_3Co_4O_9$ with Tb^{3+} and Tb^{4+} doped successfully. Scanning electron microscopy and transmission electron microscopy measurements were also performed to understand the surface morphology of the synthesized samples. Amongst the synthesized samples, $Ca_{2.5}Tb_{0.5}Co_4O_9$ exhibited a highest Seebeck coefficient of 322.9 μV/K, electrical conductivity of 155.28 S/cm, along with a lower thermal conductivity of 1.24 W/m.K at 800 K. Furthermore, it also exhibited a highest power factor of 1.62 mW/mK^2, with a high figure of merit about 1.04 at 800 K. This is the highest figure of merit that is ever reported in layered oxide-based TE materials since their discovery as shown in Figure A.2 and Figure A.3.

A.1 Publications submitted during MS study

1. **Haritha Sree Yaddanapudi**, Kun Tian, Shaing Teng and Ashutosh Tiwari, "Facile preparation of nickel/carbonized wood nanocomposite as ultra-high rate capability electrodes for environmentally friendly supercapacitors." Submitted to Nature Scientific reports.

2. **Haritha Sree Yaddanapudi**, Kun Tian and Ashutosh Tiwari, "Synthesis and characterization of nickel/carbon nanocomposite from wood as electrodes for environmental friendly supercapacitors." Materials Research Society (MRS) Fall 2016 - Abstract Accepted.

3. Ashutosh Tiwari, Shrikant Saini, Kun Tian, **Haritha Sree Yaddanapudi**. "Discovery of a new high-performance Thermoelectric Material: Terbium Calcium Cobalt Oxide (TCCO)." - U.S Patent pending.

4. Shrikant Saini, **Haritha Sree Yaddanapudi**, Kun Tian, Yinong Yin and Ashutosh Tiwari. "Terbium ion doping in $Ca_3Co_4O_9$: A step towards high-performance thermoelectric materials." - Submission in progress.

5. **Haritha Sree Yaddanapudi**, Nathan Hickerson, Shrikant Saini and Ashutosh Tiwari, "Fabrication of Transparent wood - A next generation building material" - Submission in progress.

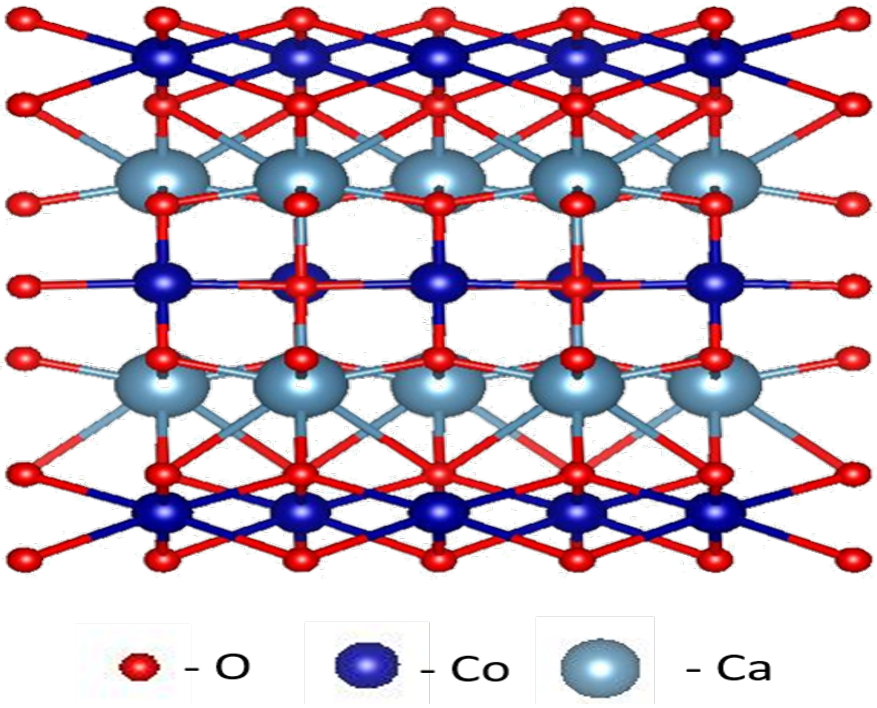

Figure A.1. Crystal structure of $Ca_3Co_4O_9$ using Vesta software.

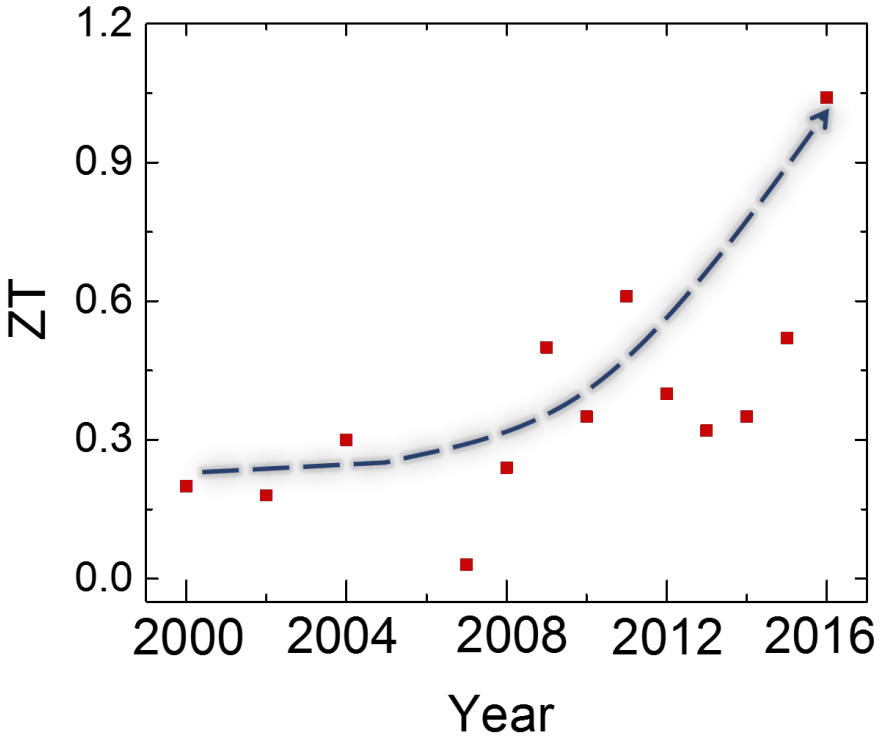

Figure A.2. Trend of ZT in $Ca_3Co_4O_9$ system from 2000 to 2016.

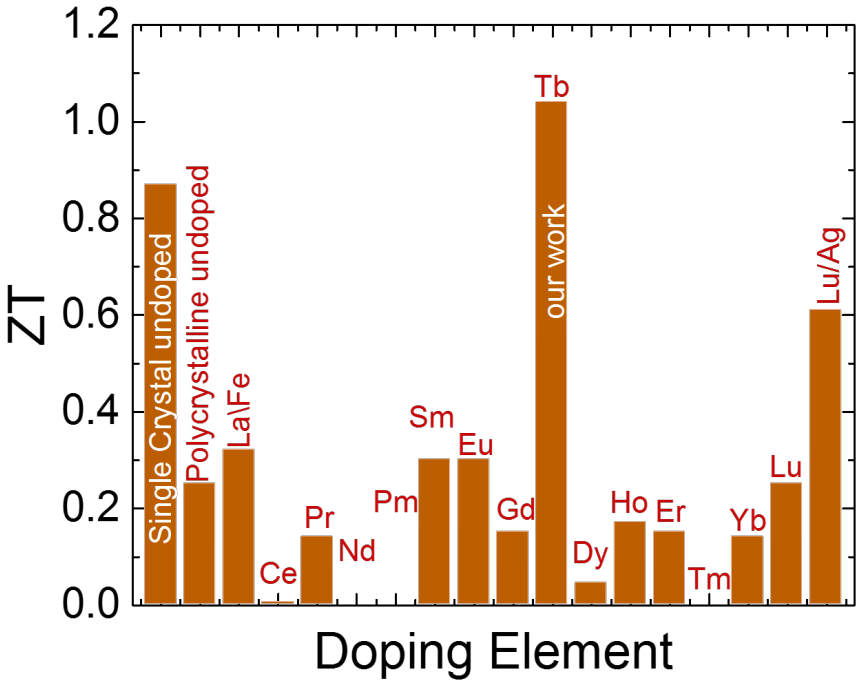

Figure A.3. ZT at 800 K for various heavy ion-doped $Ca_3Co_4O_9$ polycrystalline samples along with the present work.

APPENDIX B

TRANSPARENT WOOD, A NEXT GENERATION BUILDING MATERIAL

An environmentally friendly material that is abundantly available is wood. Wood due to its unique structure and natural growth process possesses excellent mechanical properties. These include high strength, good durability, high moisture content, and high specific gravity (72,73). Based on its structure, availability, and geographical differences wood is classified into two types soft wood and hard wood. Soft wood has a high porosity due to its faster growth. Soft wood mainly includes cedar, pine, spruce, and redwood. In contrast to soft wood, hard wood has a higher density and is denser in structure. Moreover, the longitudinal cells are shorter in length when compared to those in hard wood (74). However, both the soft and hard woods possess similar hierarchical structure. In other words, the orientation of the cells in the wood is similar.

One of the unique properties that wood possesses is its structural anisotropy. This is mainly due to the alignment of the vertical channels across the cells present in the wood which, causes it to pump ions and water for the photosynthesis process. Cells in the wood are mainly composed of cellulose, which is a long chain of polysaccharide molecules composed of at least 40%-50% glucose. It also comprises lower molecular weight polysaccharides chains called hemicellulose. Lignin is the other major component that is present in the wood. It accounts for about 25% of the wood structure. It mainly acts as a glue which helps in bonding all the wood cells together. Furthermore, lignin provides high hardness and rigidity to the wood (75). Cellulose, which is the major component in the wood, plays a vital role in development of flexible electronics for energy storage and energy harvesting. Recent investigations suggested that the cellulose extracted from wood can be used as a potential material for supercapacitors (76-78). However, further studies on environmentally friendly and benign processes for the extraction of cellulose from wood to fabricate electrodes for supercapacitors is highly necessary.

Apart from energy storage devices, wood also plays a major role in the development

of optoelectronic devices (79,80). However to make an optoelectronic device wood should be transparent to all the colors. As mentioned earlier, the main components of wood are cellulose, hemicellulose, and lignin. In contrast to cellulose and hemicellulose which are colorless, lignin possess an extremely dark color. Therefore, this dark color leads to light scattering over the visible range. One way to make the wood transparent is to bleach the wood, which helps in removing the lignin and pulp. However, since all the color, across the pores in the wood are not removed, polymer which can provide strength and transparency is impregnated into the pores of the wood, which run vertically down. Several research investigations have been conducted recently to fabricate transparent wood successfully (81,82). However, the transparent wood obtained is not environmentally friendly.

Future outlook of this thesis would also focus on the development of environmentally friendly transparent wood. In this thesis, we are proposing a unique method to synthesize transparent wood.The first step of the synthesis is to delignify the wood. Delignification is mainly done to remove the lignin present in the wood. This is performed at 120^{o}C using sodium chlorite and actetate buffer solution for about 12 hours until the wood turns white in color. Later, the delignified wood is preserved in ethanol before performing any other experiments. This delignified wood is later impregnated with environmentally friendly polymers such as polymethyl methacrylate (PMMA), Polyvinylpyrrolidone (PVP), and so forth, to retain the structure and strength of the wood thereby obtaining transparent wood structure. However, further experiments are required to prove that the proposed method is valid.

REFERENCES

[1] Wang, H.J.; Gao, Q.M.; Hu, J. High hydrogen storage capacity of porous carbons prepared by using activated carbon. *Journal of the American Chemical Society.* **2009**, *131* (20), 7016-7022.

[2] Yang, S. B.; Feng, X. L.; Ivanovici, S.; Mllen, K. Fabrication of grapheneencapsulated oxide nanoparticles: towards highperformance anode materials for lithium storage. *Angewandte Chemie International Edition.* **2010**, *49* (45), 8408-8411.

[3] Wang, Z. Y.; Zhou, L; Lou, X.W. Metal Oxide Hollow Nanostructures for Lithiumion batteries. *Advanced materials.* **2012**, *24* (14), 1903-1911..

[4] Armand, M.; Tarascon, J. M. Building better batteries. *Nature.* **2008**, *451* (7179), 652-657.

[5] Wu, H.; Yu, G.; Pan, L.; Liu, N.; McDowell, M. T.; Bao, Z; Cui, Y. Stable Li-ion battery anodes by in-situ polymerization of conducting hydrogel to conformally coat silicon nanoparticles. *Nature communications.* **2013**, 4.

[6] Park, C. M.; Kim, J. H.; Kim, H.; Sohn, H. J. Li-alloy based anode materials for Li secondary batteries. *Chemical Society Reviews.* **2010**, *39* (8), 3115-3141.

[7] Lang, X. Y.; Hirata, A.; Fujita, T.; Chen, M. W. Nanoporous metal/oxide hybrid electrodes for electrochemical supercapacitors. *Nature Nanotechnology.* **2011**, *6* (4), 232-236.

[8] Jiang, H.; Lee, P. S.; Li, C. 3D carbon based nanostructures for advanced supercapacitors. *Energy and Environmental Science.* **2010**, *6* (1), 41-53.

[9] Liu, H.; Yang, W. Ultralong single crystalline V 2 O 5 nanowire/graphene composite fabricated by a facile green approach and its lithium storage behavior. *Energy and Environmental Science.* **2011**, *4* (10), 4000-4008.

[10] Liu, J. P.; Jiang, J.; Cheng, C. W.; Li, H. X.; Zhang, J.; Gong, H.; Fan, H. J. Co_3O_4 Nanowire@ MnO_2 Ultrathin Nanosheet Core/Shell Arrays: A New Class of HighPerformance pseudocapacitive Materials. *Advanced Materials.* **2011**, *23* (18), 2076-2081.

[11] Wang, G.P.; Zhang, L.; Zhang, J.J. A review of electrode materials for electrochemical supercapacitors. *Chemical Society Reviews.* **2012**, *41* (2), 797-828.

[12] Conway, B. E. Transition from supercapacitor to battery behavior in electrochemical energy storage. *Journal of the Electrochemical Society.* **1991**, *138* (6), 1539-1548.

[13] Simon, P.; Gogotsi, Y. Materials for electrochemical capacitors. *Nature materials.* **2008**, *7* (11), 845-854.

[14] Burke, A. Ultracapacitors: why, how, and where is the technology. *Journal of power sources.* **2009**, *91* (1), 37-50.

[15] Ji, H.; Zhao, X.; Qiao, Z.;, Jung, J.; Zhu, Y.; Lu, Y.; Zhang, L.L.; MacDonald A.H.; Ruoff, R. S. Capacitance of carbon-based electrical double-layer capacitors. *Nature communications.* **2014**, 5.

[16] Schtter, C.; Ramirez-Castro, C.; Oljaca, M.; Passerini, S.; Winter, M.; Balducci, A. Activated Carbon, Carbon Blacks and Graphene Based Nanoplatelets as Active Materials for Electrochemical Double Layer Capacitors: A Comparative Study. *Journal of The Electrochemical Society.* **2015**, *162* (1), A44-A51.

[17] Ruoff, R. High Surface Area Graphene-Based Materials for Electrochemical Energy Storage. *Ecs, In 225th ECS Meeting (May 11-15, 2014).* **2014**,

[18] Raccichini, R.; Varzi, A.; Passerini, S.; Scrosati, B. The role of graphene for electrochemical energy storage. *Nature materials.* **2015**, *14* (3), 271-279.

[19] Zhang, C.; Hatzell, K. B.; Boota, M.; Dyatkin, B.; Beidaghi, M.; Long, D.; Qiao, W.; Kumbur, E. C.; Gogotsi, Y. Highly porous carbon spheres for electrochemical capacitors and capacitive flowable suspension electrodes. *Carbon.* **2014**, *77* 155-164.

[20] Rolison, D. R.; Long, J. W.; Lytle, J. C.; Fischer, A. E.; Rhodes, C. P.; McEvoy, T. M.; Bourg, M. E.; Lubers, A. M. Multifunctional 3D nanoarchitectures for energy storage and conversion. *Chemical Society Reviews.* **2009**, *38* (1), 226-252.

[21] Liu, C.; Yu, Z.; Neff, D.; Zhamu, A.; Jang, B. Z. Graphene-based supercapacitor with an ultrahigh energy density. *Nano letters.* **2010**, *10* (12), 4863-4868.

[22] Mekhilef, S.; Saidur, R.; Safari, A. Comparative study of different fuel cell technologies. *Renewable and Sustainable Energy Reviews.* **2012**, *16* (1), 981-989.

[23] OHayre, R.; Cha, S. W.; Colella, W.; Prinz, F. B. *Fuel cell Fundamentals.* John Wiley and Sons, New York. **2006**.

[24] Zhang, L. L.; Zhao, X. S. Carbon-based materials as supercapacitor electrodes. *Chemical Society Reviews.* **2009**, *38* (9), 2520-2531.

[25] Lv, S.; Fu, F.; Wang, S.; Huang, J.; Hu, L. Novel wood-based all-solid-state flexible supercapacitors fabricated with a natural porous wood slice and polypyrrole. *RSC Advances.* **2015**, *5* (4), 2813-2818.

[26] Liu, M. C.; Kong, L. B.; Zhang, P.; Luo, Y. C.; Kang, L. Porous wood carbon monolith for high-performance supercapacitors. *Electrochimica Acta.* **2012**, *60* 443-448.

[27] Cua, A.; Tancredi, N.; Bussi, J.; Barranco, V.; Centeno, T. A.; Quevedo, A.; Rojo, J. M. Biocarbon Monoliths as Supercapacitor Electrodes: Influence of Wood Anisotropy on Their Electrical and Electrochemical Properties. *Journal of The Electrochemical Society* **2014**, *161* (12), A1806-A1811.

[28] Jiang, J.; Zhang, L.; Wang, X.; Holm, N.; Rajagopalan, K.; Chen, F.; Ma, S. Highly ordered macroporous woody biochar with ultra-high carbon content as supercapacitor electrodes. *Electrochimica Acta.* **2013**, *113* 481-489.

[29] Volperts, A.; Dobele, G.; Zhurinsh, A.; Vervikishko, D.; Shkolnikov, E.; Ozolinsh, J.; Ulmane, N. M.; Sildos, I. Highly Porous Wood Based Carbon Materials for Supercapacitors. *IOP Conference Series: Materials Science and Engineering.* **2015**, *4* (77) 1, 012016.

[30] Islam, M. S.; Fisher, C. A. J. Lithium and sodium battery cathode materials: computational insights into voltage, diffusion and nanostructural properties. *Chemical Society Reviews.* **2014**, *43* (1), 185-204.

[31] Ajayan, P. M.; Zhou, O. Z. *Applications of carbon nanotubes.* Carbon nanotubes, Springer Berlin Heidelberg, **2001**, 391-425.

[32] Halper, M. S.; Ellenbogen, J. C. Supercapacitors: A brief overview. *The MITRE Corporation, McLean, Virginia, USA.* **2006**, 1-34.

[33] Zhang, L. L.; Zhao, X. S. Carbon-based materials as supercapacitor electrodes. *Chemical Society Reviews.* **2009**, *38* (9), 2520-2531.

[34] Gouy, G. Constitution of the electric charge at the surface of an electrolyte. *J. Phys.* **1910**, *9* (4), 457-467.

[35] D. L. Chapman LI. A contribution to the theory of electrocapillarity. *The London, Edinburgh, and Dublin philosophical magazine and journal of science.* **1913**, *25* (138), 475-481.

[36] Torrie, G. M.; Valleau, J. P. Electrical double layers. 4. Limitations of the Gouy-Chapman theory. *The Journal of Physical Chemistry.* **1982**, *86* (16), 3251-3257.

[37] Zhu, F. Y.; Wang, Q. Q.; Zhang, X. S.; Hu, W.; Zhao, X.; Zhang, H. X. 3D nanostructure reconstruction based on the SEM imaging principle, and applications. *Nanotechnology.* **2014**, *25* (18), 185705.

[38] Li, Hanlu and Wang, Jixiao and Chu, Qingxian and Wang, Zhi and Zhang, Fengbao and Wang, Shichang. Theoretical and experimental specific capacitance of polyaniline in sulfuric acid. *Journal of Power Sources.* **2009**, *190* (2), 578–586.

[39] Conway, B. E. *Electrochemical supercapacitors: scientific fundamentals and technological applications.* Springer Science and Business Media, New York. **2013**.

[40] Xia, X. H.; Tu, J. P.; Wang, X. L.; Gu, C. D.; Zhao, X. B. Mesoporous Co_3O_4 monolayer hollow-sphere array as electrochemical psuedocapacitor material. *Chemical Communications.* **2011**, *47* (20), 5786-5788.

[41] Alsabet, M.; Grden, M.; Jerkiewicz, G. Electrochemical growth of surface oxides on nickel. Part 1: formation of -Ni (OH) 2 in relation to the polarization potential, polarization time, and temperature. *Electrocatalysis.* **2011**, *2* (4), 317-330.

[42] Oliveira, V. L.; Morais, C.; Servat, K.; Napporn, T. W.; Tremiliosi-Filho, G.; Kokoh, K. B. Studies of the reaction products resulted from glycerol electro oxidation on Ni-based materials in alkaline medium. *Electrochimica Acta.* **2014**, *117* 255-262.

[43] Asgari, M.; Maragheh, M. G.; Davarkhah, R.; Lohrasbi, E.; Golikand, A. N. Electrocatalytic oxidation of methanol on the nickelcobalt modified glassy carbon electrode in alkaline medium. *Electrochimica Acta.* **2012**, *59* 284-289.

[44] Fleischmann, M.; Korinek, K.; Pletcher, D. The oxidation of organic compounds at a nickel anode in alkaline solution. *Journal of Electroanalytical Chemistry and Interfacial Electrochemistry.* **1971**, *31* (1), 39-49.

[45] Mabbot, G.A. An introduction to cyclic voltammetry. *Journal of Chemical education.* **1983**, *60* (9), 697-702.

[46] Li, J.; Liu, E. H.; Li, W.; Meng, X. Y.; Tan, S. T. Nickel/carbon nanofibers composite electrodes as supercapacitors prepared by electrospinning. *Journal of Alloys and Compounds* **2009**, *478* (1), 371-374.

[47] Li, H.B.; Yu, M.H.; Wang, F.X.; Liu, P.; Liang, Y.; Xiao, J.; Wang, C.X.; Tong, Y.X.; Yang, G.W. Amorphous nickel hydroxide nanospheres with ultrahigh capacitance and energy density as electrochemical pseudocapacitor materials. *Nature communications.* **2013**, *4*, 1894.

[48] Xia, X.; Tu, J.; Mai, Y.; Chen, R.; Wang, X.; Gu, C.; Zhao, X. Graphene sheet/porous NiO hybrid film for supercapacitor applications. *Chemistry–A European Journal.* **2011**, *17* (39), 10898–10905.

[49] Chen, S.; Duan, J.; Tang, Y.; Zhang Qiao, S. Hybrid hydrogels of porous graphene and nickel hydroxide as advanced supercapacitor materials. *Chemistry–A European Journal.* **2013**, *19* (22), 7118–7124.

[50] Wang, L.; Li, X.; Guo, T.; Yan, X.; Tay, B.K. Three-dimensional Ni (OH) 2 nanoflakes/graphene/nickel foam electrode with high rate capability for supercapacitor applications. *International Journal of Hydrogen Energy.* **2014**, *39* (15), 7876–7884.

[51] Tang, Z.; Tang, C.H.; Gong, H. A High Energy Density Asymmetric Supercapacitor from Nano-architectured Ni (OH) 2/Carbon Nanotube Electrodes. *Advanced Functional Materials.* **2012**, *22* (6), 1272–1278.

[52] Liu, T.; Shao, G.; Ji, M.. Electrodeposition of Ni (OH) 2/Ni/graphene composites under supergravity field for supercapacitor application. *Materials Letters.* **2014**, *122*, 273–276.

[53] Cao, L.; Kong, L.B.; Liang, Y.Y.; Li, H.L. Preparation of novel nano-composite Ni (OH) 2/USY material and its application for electrochemical capacitance storage. *Chemical communications.* **2004**, (14), 1646–1647.

[54] Ji, J.; Zhang, L.L.; Ji, H.; Li, Y.; Zhao, X.; Bai, X.; Fan, X.; Zhang, F.; Ruoff, R.S. Nanoporous Ni (OH) 2 thin film on 3D ultrathin-graphite foam for asymmetric supercapacitor. *ACS nano.* **2013**, *7* (7), 6237–6243.

[55] Syarif, N.; Tribidasari, I. A.; Wibowo, W. Modification of porous carbon with nickel oxide impregnation to enhance the electrochemical capacitance and conductivity. *Carbon.* **2004**, *42* (11), 2335–2338.

[56] Tritt, Terry M and Subramanian, MA. Thermoelectric materials, phenomena, and applications: a bird's eye view. *MRS bulletin.* **2006**, *31* (03), 188–198.

[57] Böttner, Harald. Thermoelectrics for High Temperatures: A Survey of State of the Art. *MRS Proceedings.* **2009**, *1166*, 1166–N01.

[58] Toberer, Eric S and May, Andrew F and Snyder, G Jeffrey. Zintl chemistry for designing high efficiency thermoelectric materials. *Chemistry of Materials.* **2009**, *22* (3), 624–634.

[59] Kanatzidis, Mercouri G. Nanostructured Thermoelectrics: The New Paradigm?. *Chemistry of Materials.* **2009**, *22* (3), 648–659.

[60] Li, Qiang and Lin, Zhiwei and Zhou, Juan. Thermoelectric materials with potential high power factors for electricity generation. *Journal of electronic materials.* **2009**, *38* (7), 1268–1272.

[61] Ma, Yi and Hao, Qing and Poudel, Bed and Lan, Yucheng and Yu, Bo and Wang, Dezhi and Chen, Gang and Ren, Zhifeng. Enhanced thermoelectric figure-of-merit in p-type nanostructured bismuth antimony tellurium alloys made from elemental chunks. *Nano Letters.* **2008**, *8* (8), 2580–2584.

[62] Terasaki, Ichiro and Sasago, Yoshitaka and Uchinokura, Kunimitsu. Large thermoelectric power in $NaCo_2O_4$ single crystals. *Physical Review B.* **1997**, *56* (20), R12685.

[63] Mizutani, Atsushi and Sugiura, Kenji and Ohta, Hiromichi and Koumoto, Kunihito. Epitaxial Film Growth of Li x CoO2 (0.6 x 0.9) via Topotactic Ion Exchange of Na0. 8CoO2. *Crystal Growth and Design.* **2008**, *8* (3), 755–758.

[64] Sugiura, Kenji and Ohta, Hiromichi and Nomura, Kenji and Hirano, Masahiro and Hosono, Hideo and Koumoto, Kunihito. High electrical conductivity of layered cobalt oxide Ca_3Co_4O_9 epitaxial films grown by topotactic ion-exchange method. *Applied physics letters.* **2006**, *89* (3), 032111.

[65] Sugiura, Kenji and Ohta, Hiromichi and Nomura, Kenji and Saito, Tomohiro and Ikuhara, Yuichi and Hirano, Masahiro and Hosono, Hideo and Koumoto, Kunihito. Thermoelectric properties of the layered cobaltite Ca3Co4O9 epitaxial films fabricated by topotactic ion-exchange method. *Materials transactions.* **2007**, *48* (8), 2104–2107.

[66] Ohta, Shingo and Nomura, Takashi and Ohta, Hiromichi and Hirano, Masahiro and Hosono, Hideo and Koumoto, Kunihito. Large thermoelectric performance of heavily Nb-doped SrTiO_3 epitaxial film at high temperature. *Applied physics letters.* **2005**, *87* (9), 092108.

[67] Kurita, Daisuke, Ohta, Shingo, Hiromichi, Koumoto, Kunihito et al. Carrier generation and transport properties of heavily Nb-doped anatase TiO2 epitaxial films at high temperatures. *Journal of applied physics.* **2006**, *100* (9), 096105–1.

[68] Shikano, Masahiro and Funahashi, Ryoji. Electrical and thermal properties of single-crystalline (Ca2CoO3) 0.7 CoO2 with a Ca3Co4O9 structure. *Applied Physics Letters.* **2003**, *82*, 1851.

[69] Prevel, M and Perez, O and Noudem, JG. Bulk textured Ca 2.5 (RE) 0.5 Co 4 O 9 (RE: Pr, Nd, Eu, Dy and Yb) thermoelectric oxides by sinter-forging. *Solid state sciences.* **2007**, *9* (3), 231–235.

[70] Wang, Yang and Sui, Yu and Cheng, Jinguang and Wang, Xianjie and Su, Wenhui. The thermal-transport properties of the Ca3- xAgxCo4O9 system (0 x 0.3). *Journal of Physics: Condensed Matter.* **2007**, *19* (35), 356216.

[71] Constantinescu, G and Rasekh, SH and Torres, MA and Chocarro, Cristina and Díez, JC and Madre, MA and Sotelo, A. Influence of Ca substitution by Mg on the Ca3Co4O9 performances. *Boletin de la Sociedad Española de Ceramica y Vidrio.* **2014**, *53*, (1), 41–47.

[72] Sjostrom, Eero. Wood chemistry: fundamentals and applications. *Elsevier.* **2013**.

[73] Rowell, Rogers. *The chemistry of solid wood.* American Chemical Society. **1984**.

[74] Byrne, CE and Nagle, DC. Carbonization of wood for advanced materials applications. *Carbon.* **1997**, *35* (2), 259–266.

[75] Sarkanen, Kyosti Vilho and Ludwig, Charles Heberle and others. Lignins: occurrence, formation, structure and reactions. *Lignins: occurrence, formation, structure and reactions.* **1971**.

[76] Yang, Xuan and Shi, Kaiyuan and Zhitomirsky, Igor and Cranston, Emily D Cellulose Nanocrystal Aerogels as Universal 3D Lightweight Substrates for Supercapacitor Materials. *Advanced Materials.* **2015**, *27* (40), 6104–6109.

[77] Zheng, Guangyuan and Cui, Yi and Karabulut, Erdem and Wågberg, Lars and Zhu, Hongli and Hu, Liangbing. Nanostructured paper for flexible energy and electronic devices. *MRS bulletin.* **2013**, *38* (4), 320–325.

[78] Nyholm, Leif and Nyström, Gustav and Mihranyan, Albert and Strømme, Maria. Toward Flexible Polymer and Paper-Based Energy Storage Devices. *Advanced Materials.* **2011**, *23* (33), 3751–3769.

[79] Okahisa, Yoko and Yoshida, Ayako and Miyaguchi, Satoshi and Yano, Hiroyuki. Optically transparent wood–cellulose nanocomposite as a base substrate for flexible organic light-emitting diode displays. *Composites Science and Technology.* **2009**, *69* (11), 1958–1961.

[80] Iwamoto, S and Nakagaito, AN and Yano, H and Nogi, M. Optically transparent composites reinforced with plant fiber-based nanofibers. *Applied Physics A.* **2005**, *81* (6), 1109–1112.

[81] Zhu, Mingwei and Song, Jianwei and Li, Tian and Gong, Amy and Wang, Yanbin and Dai, Jiaqi and Yao, Yonggang and Luo, Wei and Henderson, Doug and Hu, Liangbing. Highly Anisotropic, Highly Transparent Wood Composites. *Advanced Materials.* **2016**.

[82] Merindol, Rémi and Diabang, Seydina and Felix, Olivier and Roland, Thierry and Gauthier, Christian and Decher, Gero. Bio-Inspired Multiproperty Materials: Strong, Self-Healing, and Transparent Artificial Wood Nanostructures. *ACS nano.* **2015**, *9* (2), 1127–1136.